

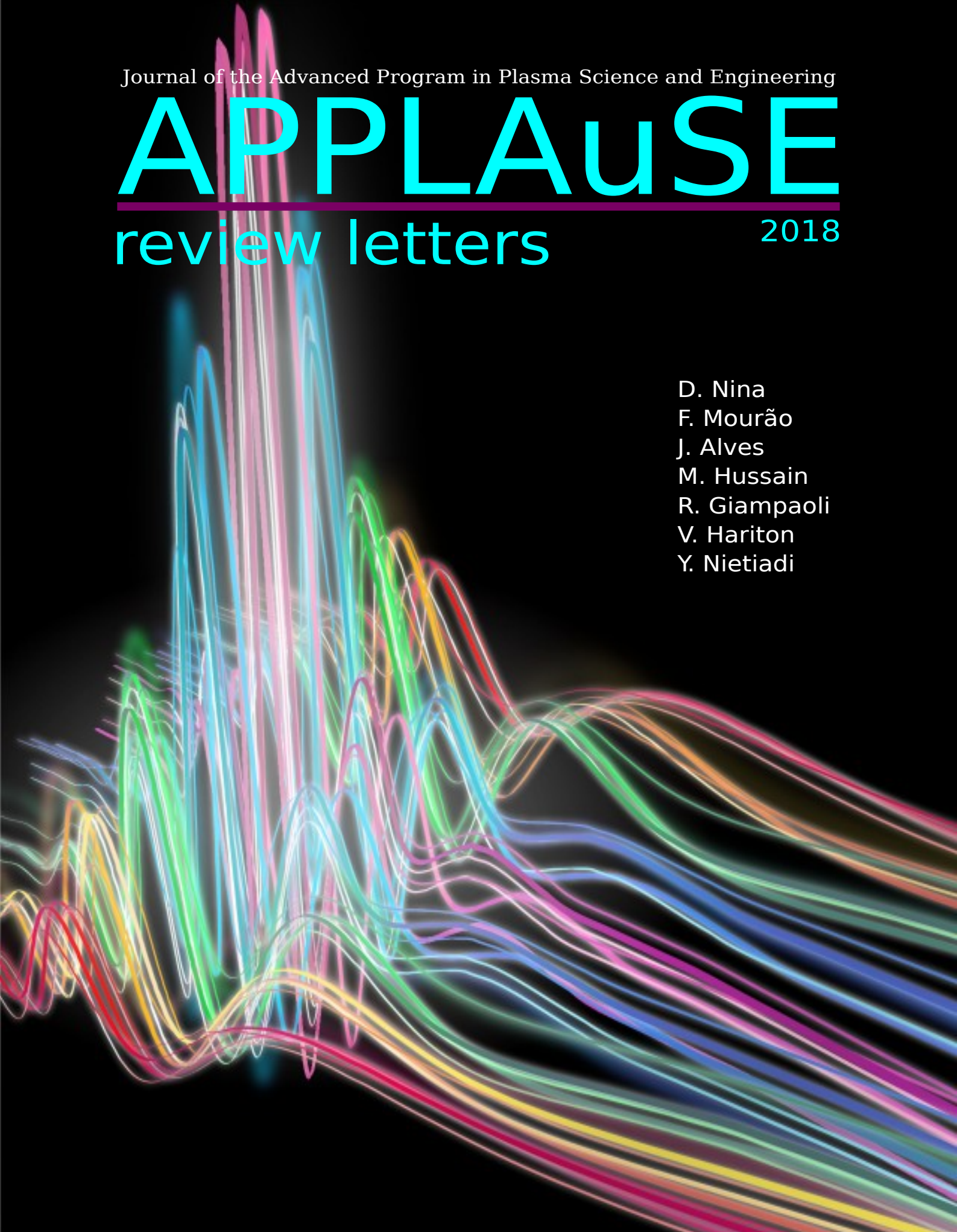
Journal of the Advanced Program in Plasma Science and Engineering

APPLAuSE

review letters

2018

D. Nina
F. Mourão
J. Alves
M. Hussain
R. Giampaoli
V. Hariton
Y. Nietiadi



APPLAuSE Review Letters

Organized and Supervised by
Dr. Marta Fajardo

Guest Editor
Duarte Nina

ARL - February 2018

← Front cover photo by Tenio Popmintchev and Brad Baxley (University of Colorado): artistic representation of a pulse spectral broadening.

→ Back cover photo - authors and chief editor. Top row, from left to right: Duarte Nina, Victor Hariton and Ruggero Giampaoli. Bottom row, from left to right: Yohanes Nietiadi, Fernando Mourão, Dr. Marta Farjado, Mukhtar Hussain and Joana Alves.



Editor Foreword

Welcome to the inaugural issue of APPLAUSE Review Letters: a peer-refereed academic journal on Advances on Plasma Physics. This journal is the result of an intensive module on Transverse Skills of the APPLAUSE Doctoral Program, a course designed to improve the APPLAUSE students academic achievement. The papers presented in the APPLAUSE Review Letters show review work on selected topics, or advances made during the Laboratory Rotations hosted by teams from the Instituto de Plasmas e Fusão Nuclear (IPFN). These papers were presented as part of the summer assignment for the course, and refereed by students and senior researchers from IPFN, who generously gave their time to the course, and to whom we are very grateful. This year's course benefited from the pioneering work led by the first APPLAUSE cohort in 2014, whom the Editors would also like to thank.

This years Guest Editor is Duarte Nina, to whom we are indebted for putting together the magazine, and for instituting the Best Figure Award. We would also like to thank all the 2018 APPLAUSE students for the work carried out for the course.

We hope that the APPLAUSE Review Letters will inspire next years cohort, by showcasing the level of maturity that could be reached, in a such a tight schedule, by first year PhD students. As the coordinator of the module, it was my pleasure and my privilege to work with the 2018 APPLAUSE students.

Marta Fajardo

Instituto de Plasmas e Fusão Nuclear (IPFN), Instituto Superior Técnico

Email: marta.fajardo@tecnico.ulisboa.pt



Best Figure Award

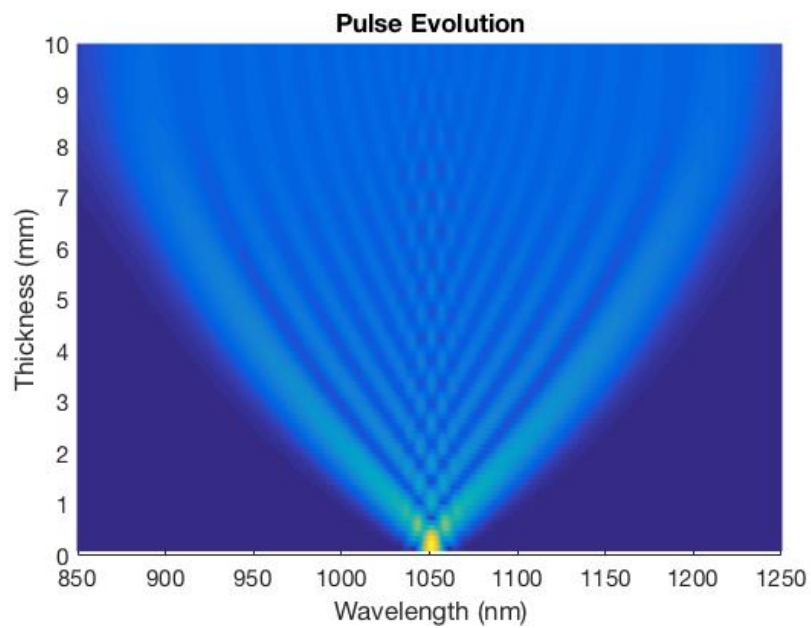


Figure 3a: Spectral evolution of a 200 fs pulse inside the material of two different time scale pulses.

Every year, from among all the submitted articles, the participants select a winner for the Best Figure Award of that APPLAuSE Review Letters edition. We are glad to announce that this year's winner is Victor Hariton!

This year's awarded figure shows us that, even when performing a task like simulations or data analysis, we should not just look for conclusions and results, but should also strive to find beauty

Contents

Editor Foreword	iii
Best Figure Award	v
Table of Contents	vi
1 Analysing Data from JET Gamma-ray Cameras, Duarte Nina	1
1. Introduction	2
2. Code	2
3. Examples	5
4. Conclusions	7
2 Machine Control and Monitoring at ISTTOK, Fernando Mourão	9
1. Introduction	10
2. New Slow Control System	12
3. Final Remarks	14
A. Tables	16
B. Figures	17
3 Temperature determination using laser interferometry, Joana Alves	19
1. Introduction	20
2. Experimental Setup	20
3. Phase extraction	20
4. Abel inversion	21
5. Results and discussion	22
6. Conclusions	27
4 Optimization of High Harmonic Generation in Gases, Mukhtar Hussain	29
1. Introduction	30
2. Experimental setup and optimization of HHG	30
3. Results and Discussions	31
5 Microwave plasmas graphene synthesis, Ruggero Giampaoli	37
1. Introduction	38
2. Synthesis of pure graphene: setup description	38
3. Results and discussion	39
4. Estimation of the plasma temperature by using the rotational spectrum of OH ⁻	41
5. Conclusions	42
6 Nonlinear processes for ultrashort pulse broadening, Victor Hariton	45
1. Introduction	46
2. Theory of bulk material	46
3. Matrix formalism	47
4. Split-step method for time domain	49
5. Experimental setup and results	51
6. Conclusion	52

7	Survivability Test of DEMO Diagnostics Components, Yohanes S. Nietiadi	55
1.	Introduction	56
2.	Methodology	56
3.	Results and Discussion	56
4.	Conclusion	61

Analysing Data from JET Gamma-ray Cameras



Duarte was born in Lisbon, Portugal, in 1992. From early on, he decided that he wanted to follow science and so he joined Physics Engineering at IST. He was awarded his MSc in 2016, with a thesis on Modelling Chlorine Plasmas, supervised by Prof. Vasco Guerra. He was accepted into the APPLAuSE program in 2017 and is now working on his PhD.

During his years at IST, he was also part of NFIST, an outreach student association with several events per year. Duarte is an avid gamer and reader and has started to learn karate.

Duarte Nina

Instituto de Plasmas e Fusão Nuclear (IPFN), Instituto Superior Técnico, Avenida Rovisco Pais, 1049-001 Lisboa, Portugal

E-mail: duartenina@tecnico.ulisboa.pt

February 2018

Abstract.

The existing codes for processing and analysing data from the JET Gamma-ray cameras were joined, expanded and improved, adding new features such as background subtraction. Several shots were studied to understand the possibilities and limitations of the algorithms. Furthermore the code was successfully tested inside JET's servers.

1. Introduction

The Joint European Torus (JET) is a tokamak built in the 1980's to study fusion plasmas. It has been upgraded, improved and expanded several times since its initial iteration. Diagnostics are one of the most important parts of JET (and any reactor), since they help to control the plasma and are the largest source of data for studying a plasma. Gamma-ray spectroscopy is a diagnostic which gives an insight on the behaviour of fast ions, and since these ions can have a large effect on the entire plasma, this diagnostic can be a strong tool to both control and understand fusion plasmas.

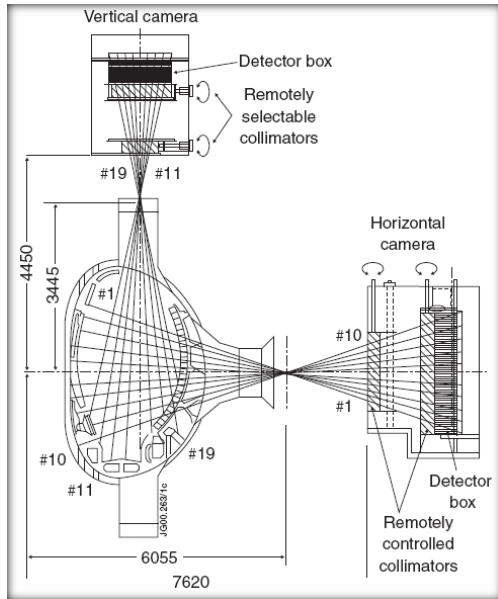


Figure 1: Position of the Gamma-ray cameras on the vessel [1].

At JET there are two gamma-ray cameras as shown in figure 1: one array with 10 detectors, looking at the plasma horizontally; and another with 9 detectors, looking vertically at the plasma. These cameras use LaBr_3 detectors that has a good energy resolution at the high energies photons created by the fast ions[3].

The detectors are controlled by several electronic boards that run on a high-frequency (in the megahertz range) clock. To reduce the amount of data stored, and for an easier data post-processing, the boards pre-process the raw data in real-time. By using the Digital Trapezoidal Shaper (DTS) method[2], any peaks found are stored only as a timestamp of the current cycle number and an energy. In figure 2, we see an example of the DTS method, converting the raw data (in black) to a processed signal (in red). The peaks of the processed signal are saved, and that is the data that the code shown here analyses.

2. Code

The code was written using Python with the help of the libraries NumPy, for mathematics, and Matplotlib, for graphics. Python was used due to its ease of use for both programmer and final user, and also due to its availability in JET's server. To guarantee that the program is able to run in most systems, it was written as compatible for both Python 2.x and 3.x.

There were already two existing codes, with limited features, dealing with the two sizes of the timestamp (see section 2.1.). These codes were joined into a single program, and expanded to allow for new features.

The program is a command line-based utility which receives a shot number, reads the respective raw data and outputs a series of data files with the information that the user might need. There are also a large number of

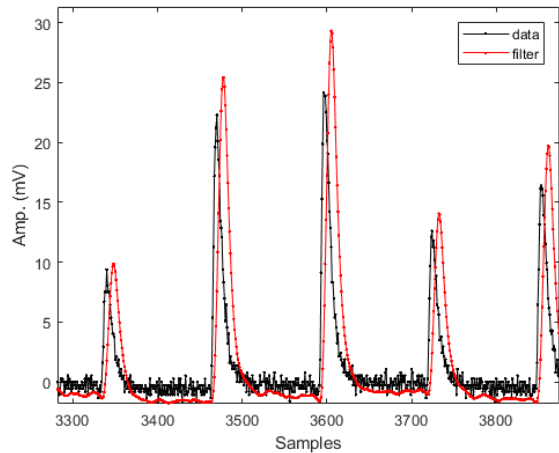


Figure 2: Example of the Digital Trapezoidal Shaper method [2].

options available, from choices in the graphs plotted to the parameters of the Analog-to-Digital-Converter (ADC) used with the detector.

2.1. Data Formatting

The recorded data is stored in a 64 bit word for each event. The previous detector ran with a slower clock (around 2.5 MHz) and its timestamp was small enough to fit in an unsigned 32 bit integer for the duration of the shots. With the upgrade to the new detector, which allows a higher clock speed (of around 200 MHz), the space reserved to timestamp was increased to the full 48 bit available.

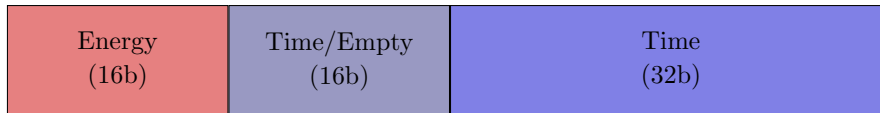


Figure 3: Sections of the 64 bit word for a recorded event. The middle sector is either empty or part of the timestamp depending on the version of the board used.

The data file is firstly read as columns of 16, 16 and 32 bits, the first of which is assigned as energy. In the case of the 32 bit timestamp, the third column is directly assigned as time. NumPy, by default, can read files in the format above, but does not recognize unsigned integers of 48 bits.

To obtain the 48 bit timestamp, the file is read again as just a column of 64 bits. The energy sector is ignored by zeroing it out with a bitmask, i.e., performing an AND operation with a binary number detailing which are the needed bits. The timestamp is then retrieved by bitshifting the result towards the 48 bit since the energy sector are located in the least significant bits.

2.2. Time Array

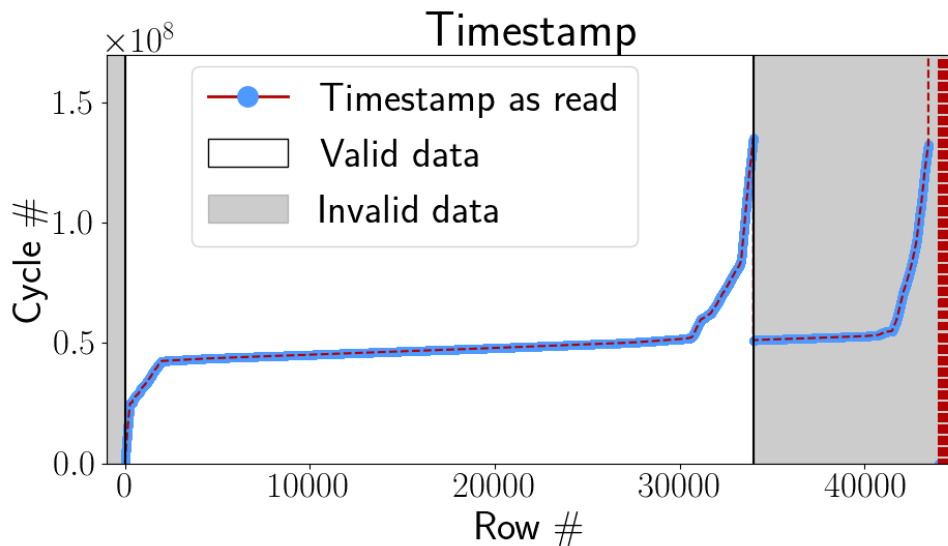


Figure 4: How to select the data by looking at the evolution of the timestamp. Valid data is defined by the section where the timestamp is always increasing.

Since the memory of the board is not always cleaned before a new shot, it is necessary to figure out what parts of the file are the actual results from the shot. This is done with the simple method of looking at the timestamp and finding when it stops increasing. In figure 4, the timestamp of a sample shot is shown. The valid data is presented

with a white background, while the invalid data has a grey background. In this particular case, it is possible to recognize the data from a previous shot in the grey section, followed by random data.

To convert the timestamp, which is the number of the cycle when the event happened, to the correct time, in seconds, the following expression is used:

$$t[s] = \frac{t_{stamp}}{f_{clock}[Hz]} + t_{delay}[s] \quad , \quad (1)$$

where t_{stamp} is the cycle number, f_{clock} is the clock frequency in Hz, and t_{delay} is the delay, in seconds, between the start of the shot and the start of the acquisition.

2.3. Energy Array

The next step is to interpret the energy data to obtain the energy in keV. This is done by calibrating each detector, i.e., each channel, with a well-known radioactive source. The results of such a run will show clearly defined peaks for which there are known and precise energies, allowing the creation of a linear calibration

$$E[keV] = a \cdot n_{channel} + b \quad , \quad (2)$$

where a and b are the parameters of the calibration. These parameters can be stored in a single file to then be accessed when needed.

The details of the ADC (number of bits and range), and the calibration define the bins of an histogram which is then filled with the energy data, obtaining a number of counts for each energy.

2.4. Background Subtraction

One of the features of the new version of the code is the option to obtain the counts of the background radiation and subtracting them from the time periods being studied. The user defines a time period where there is only background radiation and then a number of time periods of interest (named as Events).

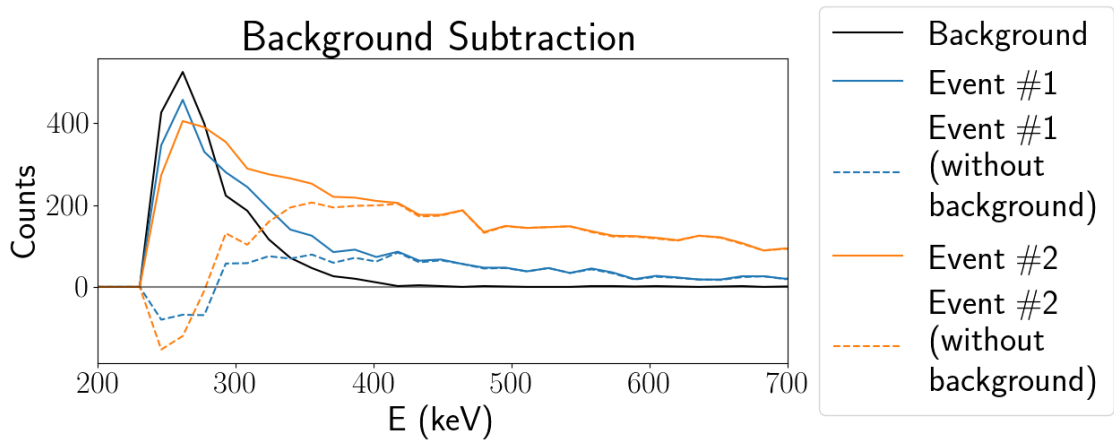


Figure 5: Two examples of background subtraction using total area as a normalization function. In black the background spectrum, in solid the spectrum of two time periods and in dashed their spectrum with the background subtracted.

The first step is then to choose and create a normalization function of the histogram, function which is, by default, the integral area of the histogram. Many other functions were explored, such as the sum of counts or the highest peak, and several are still available as an option, since different functions have different advantages and disadvantages.

Each histogram (for the background and the events) is then normalized to itself and the normalization factor used is stored. In this way, the normalized background can be subtracted from each of the normalized events. The number of counts of the events is then recovered by multiplying the result of the previous subtraction by the stored normalization factor.

An example using this method is shown in figure 5, where the background is presented as black, the original events as solid blue and orange lines and the events with the background subtracted as the dashed lines. It is possible to see one of the disadvantages of the area of the histogram, where in the low energy photons the resulting counts are negative, which is not physically correct. However, in most cases, the energies being studied are towards the high end, where the error of this method is minimized.

2.5. Output

After running the code, the user will find two new folders, ‘images’ and ‘out’. The ‘images’ folder contains graphs for each channel that allow to quickly recognize areas of interest and problems (see section 3.1.). The ‘out’ folder includes data files with all the times and energies for each channel and a single data file with the counts of the requested time periods and energy windows for all channels.

3. Examples

To understand the possibilities and limitations of the code, several shots were studied. For most of the following examples, detector 15 was chosen to present the result.

3.1. Typical Shot

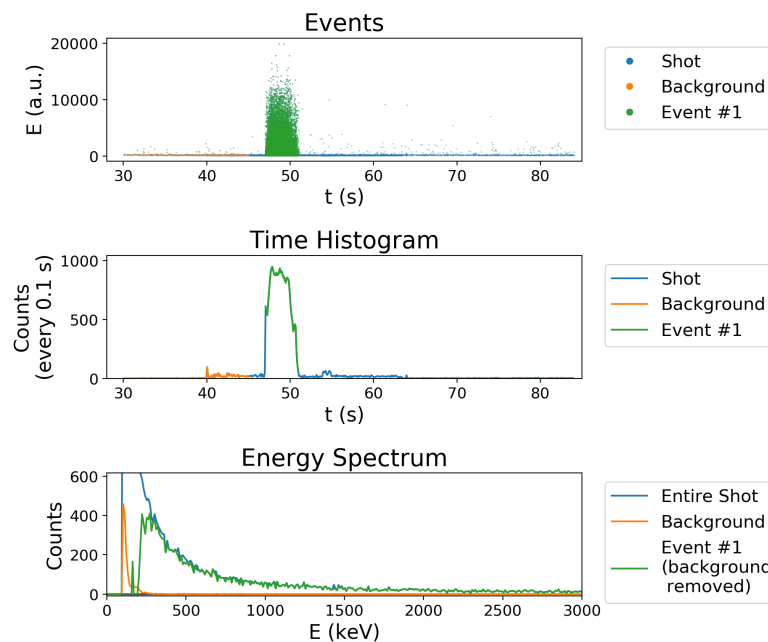


Figure 6: Example output of the code for a typical shot (detector 2 for shot 91975).

In figure 6, the default output for detector 2 of a typical shot (91975) is shown. The default graph is divided in three sections. On top, all the captured photons are shown, in time and energy, highlighting both the areas with more counts and with higher energies. In the middle, an histogram of the times is shown, showing a clear picture of the periods with the highest counts. And finally, at the bottom, the energy spectrum is shown for the entire shot, the background and any request time periods, the latter having the background already subtracted.

3.2. Calibration Shots

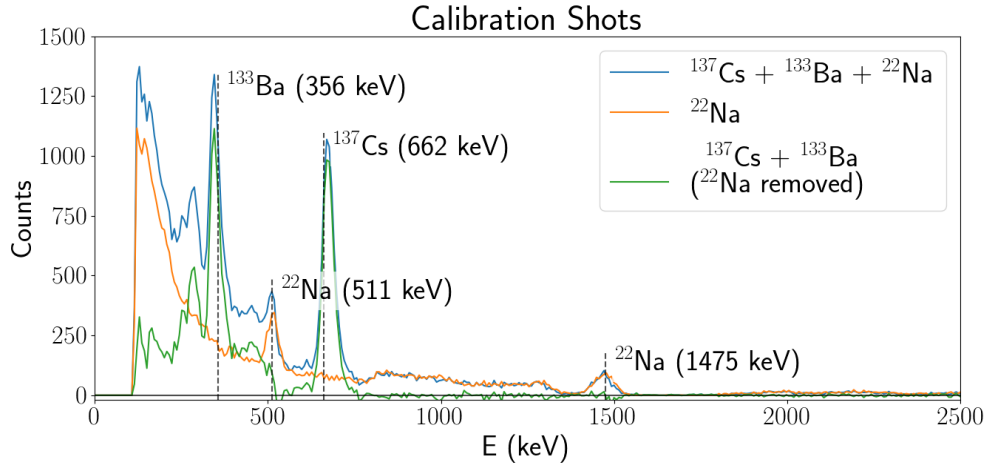


Figure 7: Energy spectrum of the calibration shots, with relevant decay peaks marked (detector 15).

After the new detector was installed, several calibration shots were made, two of which are shown in figure 7, as blue and orange. The blue line was obtained with sources of Caesium-137, Barium-133 and Sodium-22, while the orange line had just the Sodium-22 source. The green line was obtained by defining the shot with just Sodium as background to the other shot.

It is possible to identify the known peaks of each of the sources (labelled in the graph with source and energy). Also interesting to note is that the background subtraction returns the expected result, with the Sodium peaks not being present.

3.3. Spatial and Temporal Differences

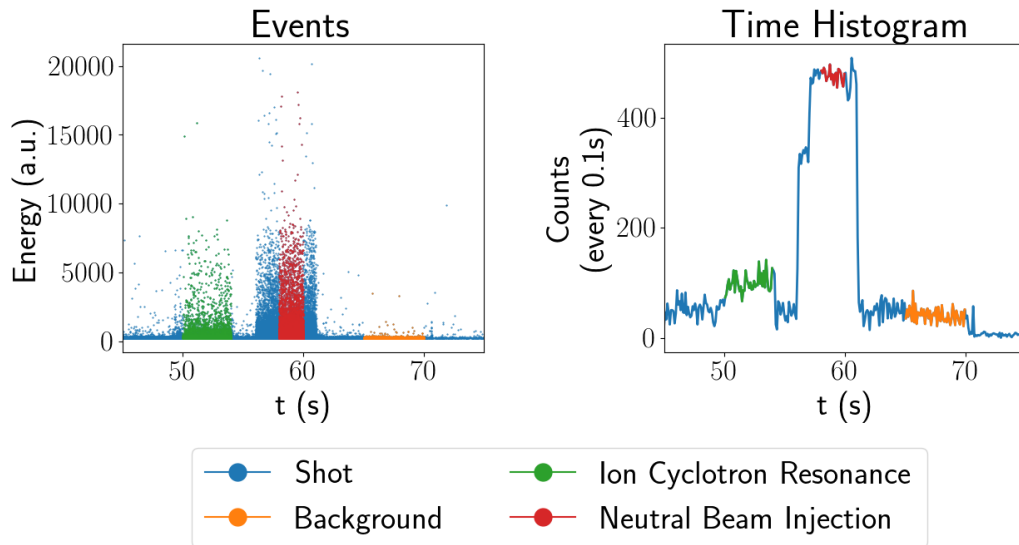


Figure 8: Differences in counts and energies for both heating methods (detector 15).

The final example is an older shot (81852), where two heating methods were used, first the Ion Cyclotron

Resonance (ICR, in green) followed after a delay by the Neutral Beam Injection (NBI, in red). This shot was chosen to highlight the option of choosing multiple time periods to study in the same shot. In figure 8, the captured photons and the number of counts summed every 0.1s are shown. From those graphs, it is possible to see that the NBI creates higher counts, and with average higher energy.

In figure 9, the counts of high energy photons (between 2.3 MeV and 7 MeV) are shown for both heatings and for each of the detectors. As expected, NBI creates higher counts across the entire plasma. As for position, both heating methods present the same overall shape. The horizontal cameras show the expected distribution, with higher counts in the centre of the plasma. The vertical cameras show a similar figure, with the exception of channels 18 and 19. This difference is usually due to high radiation counts for non-plasma sources.

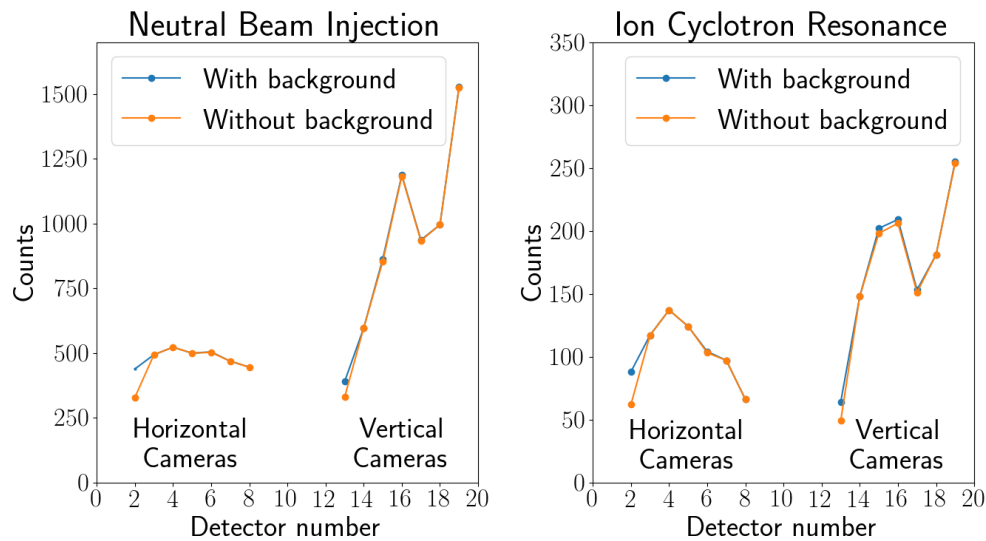


Figure 9: Differences in the number of photons with energies between 2.3 MeV and 7 MeV, for both position and heating method (detector 15).

4. Conclusions

The existing codes to process the raw data were expanded and improved, joining them into a single package that has a large array of options. Among the several new features, the background subtraction is highlighted, since it allows for a more precise count of the events being studied. The code is also faster, and requires less memory.

To test and verify the code, it was run in JET's own servers, obtaining the same results. Several shots, including a calibration shot, and shots with more than one event, were studied, and obtaining good and expected results.

In the future, it would be interesting to continue improving the tools available in the code. In particular, the background subtraction method still has some problems, such as negative counts in some energies. Another important feature would be to allow the user not to have the raw data already, by fetching the required shot directly from JET's servers. And finally, the code should be made available to the public as a polished and easy to use package.

References

- [1] V.G. Kiptily et al. ' γ -ray diagnostics of energetic ions in JET'. In: *Nuclear Fusion* 42.8 (2002), p. 999. URL: <http://stacks.iop.org/0029-5515/42/i=8/a=308>.

- [2] A. Fernandes et al. ‘New {FPGA} based hardware implementation for {JET} gamma-ray camera upgrade’. In: *Fusion Engineering and Design* 128 (2018), pp. 188 –192. ISSN: 0920-3796. DOI: <https://doi.org/10.1016/j.fusengdes.2018.02.038>. URL: <https://www.sciencedirect.com/science/article/pii/S092037961830139X>.
- [3] D. Rigamonti et al. ‘Performance of the prototype LaBr3 spectrometer developed for the JET gamma-ray camera upgrade’. In: *Review of Scientific Instruments* 87.11 (2016), 11E717. DOI: 10.1063/1.4961060. eprint: <http://aip.scitation.org/doi/pdf/10.1063/1.4961060>. URL: <http://aip.scitation.org/doi/abs/10.1063/1.4961060>.

Machine Control and Monitoring at IST tokamak (ISTTOK)



Fernando Mourão was born on May 26th 1986, in Porto. Raised in Espinho, where he finished his basic education. He graduated from the Faculty of Engineering of the University of Oporto (FEUP), in 2010, with a MSc degree in Mechanical Engineering. Started working at the Institute of Science and Innovation in Mechanical and Industrial Engineering (INEGI), in 2010, as a researcher in the Wind Energy group, becoming a project manager in 2014.

His interest in nuclear fusion made him start a part-time PhD in Physical Engineering, at FEUP, in 2016. Later that year he left his job and applied for the APPLAuSE program, at IST. In 2017 enrolled as a student in the PhD program as part of the cohort 4.

Fernando Mourão

Instituto de Plasmas e Fusão Nuclear (IPFN), Instituto Superior Técnico, Avenida Rovisco Pais, 1049-001 Lisboa, Portugal

E-mail: eng.fernando.mourao@gmail.com

February 2018

Abstract.

The ISTTOK supervisory and operational control systems for the vacuum, power and plasma conditioning are presently being upgraded to the Experimental Physics and Industrial Control System (EPICS) environment. The objectives of this “LAB Rotation” were: to obtain practical, hands-on specific experience in the methodology (modelling, analysis and design) and tools (hardware, software) of control and data acquisition system for industrial and laboratory environments; and to help in the developing and commissioning of the new control nodes needed to replace the outdated equipment, which can no longer be supported. To this purpose we were able to develop a new slow control system unit to remotely operate and control the vacuum pumps and to implement a new finite state machine, as well has to design new graphical user interfaces (GUI's), using the Control System Studio (CSS) software, for the operation of the new system.

1. Introduction

The ISTTOK slow control system is being upgraded in order to transition from the old control system based on the EDWARDS controller, which is no longer supported, to an EPICS based environment. This is a powerful framework used by many international experiments, including ITER, to implement control systems.

This report will focus on the launching of a new vacuum control unit, based on the EPICS environment, which will allow for the remote operation of the vacuum pumps and electro valves, as well as in the implementation of a new EPICS server and finite state machine.

1.1. Experimental Physics and Industrial Control System (EPICS)

The Experimental Physics and Industrial Control System (EPICS) is based on a set of software components and tools that allows developers to create control systems. This framework uses Client/Server and Publish/Subscribe techniques, allowing it to communicate between various computers. The servers (called Input/Output Controllers or IOC's) allow a client to access and pass information, through the Channel Access (CA) network protocol, that uses TCP/IP and UDP protocols, to the Process Variables (PV's), defined in the EPICS database and that are associated with all the control system components. The basic components are:

- **OPI: the Operator Interface.** We used CSS in the design of the Graphic User Interface (GUI);
- **IOC: the Input/Output Controller.** Any platform that can run and support all of EPICS software components;
- **LAN: Local Area Network.** This is the communication network which allows the IOCs and OPIs to communicate. EPICS provides a software component, Channel Access, which provides network transparent communication between a Channel Access client and an arbitrary number of Channel Access servers. [4]

A more detailed view of an EPICS IOC is presented in figure 1.

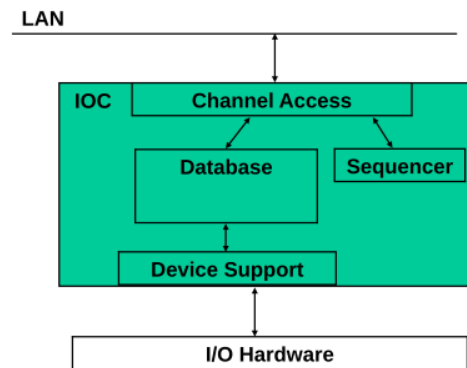


Figure 1: Major software components of an IOC [5]

These modules and extensions allow us to implement all the features of EPICS. In the Database we define the Process Variables (PV's), which are associated with the different components of the control system (monitoring signals, control signals, pressure sensors, etc). These PV's are coded as records in the necessary file. The Sequencer allows us to implement a finite state machine using State National Language (SNL) coding. This allow us to implement sequences based on control tasks performed on the system, that are triggered depending on monitoring signals, user inputs or a given time delay. Through the Device Support we can implement modules like the AsynDriver which allows the IOC to interact with the physical system by specifying different communication protocols.

2. New Slow Control System

2.1. New System Requirements

To meet the stated requirements a new vacuum control unit was built at IPFN, that connects to the vacuum pumps and also to the electro valve. The control of the turbomolecular pump is done through the SEIKO unit controller. We were able to identify four monitoring signals in this controller: the power to the controller, the emergency signal, indication that the pump's motor is accelerating and the signal that indicates the pump reached normal operation; and also four control signals: to turn the controller on, turn the controller off, turn the turbomolecular pump motor on and to turn the turbomolecular pump off.

The new vacuum control unit has a new EPICS IOC Server running, where a new state machine is already implemented. The new control unit for the slow control vacuum system was developed and assembled by Professor Bernardo Carvalho and Rui Dias at IPFN and it's comprised of:

- **a Raspberry Pi, running a linux distribution.** It also has a USB RS485 port for monitoring pressure (to be connected soon);
- **an Interface Board, Velleman k8000.** Connected to raspberry Pi through I2C interface; 8 isolated output connected to the relays (6 relays installed for the rotatory control, 2 in use); 4 isolated outputs connected to SEIKO unit controller; 4 isolated inputs connected to SEIKO unit controller;
- **Indicator leds for the relays in the front panel.**
- **24 V power supply.**

The control unit is shown in figure 3



Figure 3: Inside components of the new control unit

2.2. Design of the State Machine

For the implementation of a new finite state machine we needed to define the proper starting and stopping sequence of the vacuum pumps.

We needed to create two extra state sets, defining multiple states in each one. The first change was to the already implemented state machine. When the sequencer is started, the control system checks if the turbomolecular pump controller is on, if not, this is turned on. After the request of the user to begin the starting sequence, the control system turns the rotatory pump on. A time delay of 5 seconds is observed and then the electro valve is opened. The next step needs the user input. There is a manual valve at the exhaust of the turbomolecular pump

that needs to be opened. After this the user sets the state of this manual valve in the interface panel and the machine proceeds to the next state. There it stays, until the primary pressure goes below $3e-3$ mBar, after which the turbomolecular vacuum pump is turned on. The pump starts accelerating. When the normal operation signal is on, the machine is ready to proceed to the Process state. From the Process state, when the user gives the order to initiate the stopping sequence, the turbomolecular pump is turned off and we can see that the pressure in the system starts to increase. After the pressure reaches a certain level, meaning the pump has decelerated to a given level, the operator must close the manual valve and give this input to the control system. After this the machine holds for 5seconds before closing the electro valve. After another 5 seconds delay the rotatory pump is turned off and the machine is at the Stopped state again. The flow diagram for the implemented state machine is presented in figure 4.

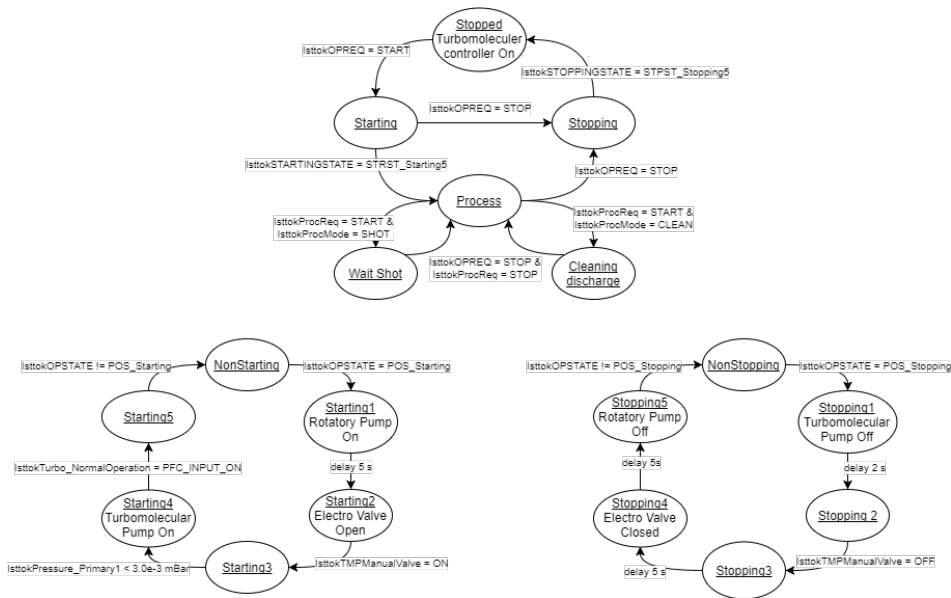


Figure 4: Flow diagram for the new finite state machine

2.3. Implementation of the New IOC Server

The new EPICS IOC Server was implemented in the Raspberry Pi of the new vacuum control unit. We followed the building procedure explained in the IPFN’s wiki page, defining all the necessary paths and modules in the site configuration files, building the Asyn and SNL modules needed for the Device Support and the Sequencer, respectively.

The communication of the I2C Interface Board with the Raspberry’s IOC is implemented with the EPICS modules ASYN STREAM and drvAsynI2C. The I2C communication protocol with the velleman board is coded in protocol file name pcf8574.proto.

We needed to declare all of the Process Variables regarding : all the states in the state machine; all the control and monitoring signals of the turbomolecular pump controller unit; and the rotatory pump and electro valve. The PV’s are coded in the database files ISTTOKvacummPumps.db and ISTTOKstates.db. The list of the PV’s created is presented in Appendix A.

The programming of the Sequencer script, where the finite state machine is implemented was written in SNL and is coded in the sequencer file name IsttokSeqExec.stt.

2.4. Graphical User Interface (GUI) Control Panels

We developed two GUI’s to be used by the ISTTOK operators. These monitoring and control panels were developed based on the work performed by Doctoral Fellow MSc Paulo F. Carvalho, as part of his PhD work, in collaboration

with the ISTTOK team. [8]

One was designed for the user to have control of the rotatory pump, the rotatory pump's electro valve and the turbomolecular vacuum pump and controller unit, as well as receive the input from the pressure and temperature sensors of the system. This also allowed us to perform a debug on the new vacuum control unit, to see if the commands were being passed to the interface board and consequently to see if the turbomolecular pump was being turned on and off when we passed the commands to the new control unit. The interface panel can be seen in figure B.1, in the appendix.

The second user interface panel allows the user to initiate the finite state machine sequence, see what actions are being taken, perform some necessary input to the IOC server installed in the Raspberry Pi and read information about the pressure and temperature in the system. Figure B.2 shows the developed interface panel and can be consulted in the appendix.

The GUI's are already installed in the control computer at ISTTOK.

3. Final Remarks

3.1. Achieved Goals

Overall we can say that the goals proposed for this laboratory rotation were achieved:

- The new control unit was installed in ISTTOK; The remote control of the turbomolecular vacuum pump was tested and is operational;
- A new EPICS IOC Server is running in the Raspberry Pi;
- A new finite state machine for the automated starting and stopping sequence of the vacuum pumps is implemented;
- The GUI's are installed in the operator computer.

3.2. Future Work

Although the new slow control vacuum control unit is already installed in ISTTOK, there is still some tasks that need to be performed:

- Upgrade the sequence for the case of emergency shut down;
- Upgrade the GUI's;
- Implement the AutoSave module in the EPICS IOC;
- Connect the rotatory pump and electro valve to the new control unit;
- Connect pressure sensors to the new control unit's IOC;
- Update the Wiki page of IPFN's.

References

- [4] et al. Martin R. Kraimer. *EPICS Application Developer's Guide, EPICS Base Release 3.14.12.5*. URL: <https://epics.anl.gov/base/R3-14/12-docs/AppDevGuide.pdf>.
- [5] John Maclean. *Introduction to EPICS*. Ed. by Argonne National Laboratory. URL: https://epics.anl.gov/docs/USPAS2014/1-Monday/EPICS_Intro.pdf.
- [6] Kay Kasemir and Gabriele Carcassi. *Control System Studio Guide: For installers and maintainers of CSStudio*. Ed. by Oak Ridge National Laboratory. URL: http://cs-studio.sourceforge.net/docbook/css_book.pdf.

- [7] URL: http://metis.ipfn.ist.utl.pt/FUSION_Collaborations/ISTTOK/Slow_control.
- [8] Paulo F. Carvalho et al. 'EPICS IOC module development and implementation for the ISTTOK machine subsystem operation and control'. In: *Fusion Engineering and Design* 86 (6-8 2011), pp. 1085–1090. URL: <https://doi.org/10.1016/j.fusengdes.2011.03.100>.

A. Tables

Table A.1: List of the Process Variables defined in ISTTOKvacummPumps.db.

PV Name	PV Type
ISTTOKrpi:central:RotatoryPump	bo
ISTTOKrpi:central:RotatoryValve	bo
ISTTOKrpi:central:TMPControllerOn	bo
ISTTOKrpi:central:TMPControllerOnInv	calcout
ISTTOKrpi:central:TMPControllerOff	bo
ISTTOKrpi:central:TMPControllerOffInv	calcout
ISTTOKrpi:central:TMPMotorOn	bo
ISTTOKrpi:central:TMPMotorOnInv	calcout
ISTTOKrpi:central:TMPMotorOff	bo
ISTTOKrpi:central:TMPMotorOffInv	calcout
ISTTOKrpi:central:Turbo_PW_Ind	bi
ISTTOKrpi:central:Turbo_Emergency	bi
ISTTOKrpi:central:Turbo_Acceleration	bi
ISTTOKrpi:central:Turbo_NormalOperation	bi
ISTTOKrpi:central:TMPManualValve	bo

Table A.2: List of the Process Variables defined in ISTTOKvacummPumps.db.

PV Name	PV Type
ISTTOKrpi:central:OPSTATE	mbbi
ISTTOKrpi:central:OPCALCSTATE	calc
ISTTOKrpi:central:OPREQ	bo
ISTTOKrpi:central:PROCESS-MODE	bo
ISTTOKrpi:central:PROCESS-REQ	bo
ISTTOKrpi:central:AUTHORISATION	bo
ISTTOKrpi:central:PULSE-NUMBER	longout
ISTTOKrpi:central:COUNTDOWN	longout
ISTTOKrpi:central:COUNTER	calc
ISTTOKrpi:central:CurrentTime	stringin
ISTTOKrpi:central:TraceMessage	stringout
ISTTOKrpi:central:STARTINGSTATE	mbbi
ISTTOKrpi:central:STOPPINGSTATE	mbbi

B. Figures

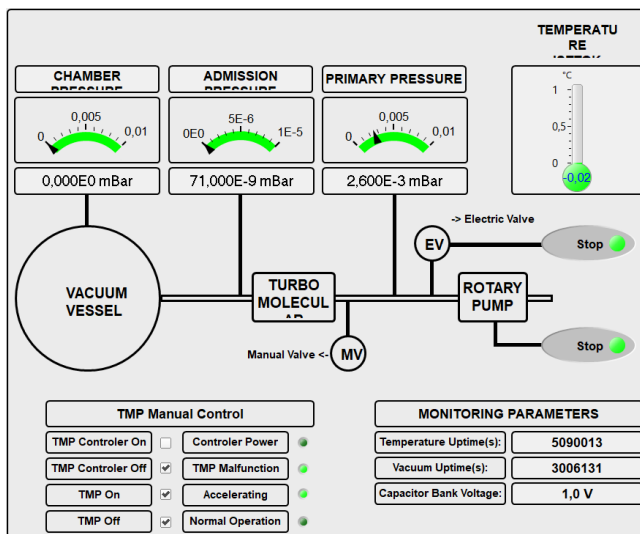


Figure B.1: GUI for the “manual” control of the slow control vacuum system

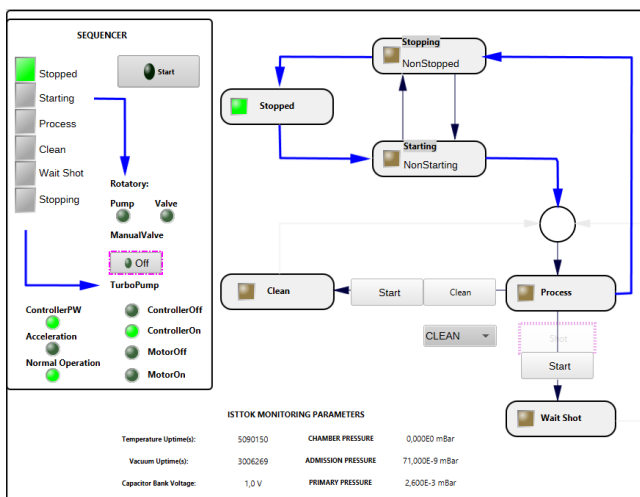


Figure B.2: GUI for the finite state machine

Determination of a temperature distribution using laser interferometry



Joana obtained her MSc degree in Physics Engineering in 2015 at the Faculty of Science and Technology of the New University of Lisbon. Her MSc thesis work was performed at IPFN's Group for Lasers and Plasmas, aiming at the development of a novel high-power, ultrashort laser system at the Laboratory of Intense Lasers. She has specialized in ultrashort laser pulse characterization and dispersion management for broadband pulses.

After her graduation, Joana joined ESA's Opto-Electronics Section at the European Space Research and Technology Centre, Noordwijk, Netherlands, for two years, as a Young Graduated Trainee. Here she continued performing experimental work with intense lasers and with a wide range of optical characterization techniques within the research topic of Laser Induced Damage Analysis.

Besides science, she has complementary studies in music and arts. She also likes to swim, dance and to travel.

Joana Alves

GoLP / Instituto de Plasmas e Fusão Nuclear (IPFN), Instituto Superior Técnico, Avenida Rovisco Pais, 1049-001 Lisboa, Portugal

E-mail: joanacasanova@tecnico.ulisboa.pt

February 2018

Abstract.

Optical plasma diagnostics are of key importance for measuring some of the plasma properties in the field of laser-plasma interactions. The aim of this lab rotation was to explore one of such diagnostics - the laser interferometer. By assembling an experimental setup and developing a computer algorithm for the reconstruction of a temperature profile, measurements and data analysis were performed.

1. Introduction

The interaction of intense laser pulses with underdense targets, like gas jets, has interesting applications in areas such as particle acceleration [9], x-ray lasers [10, 11], plasma channelling [12] and photon acceleration [13]. The characterization of the density structure of the underdense region can yield important information on the processes resulting from such interactions. A powerful tool to retrieve such information is laser interferometry. Here, the deviation of the fringes from straight lines is proportional to the phase shift of the probe light due to the presence of the gas. This allows the determination of the phase shift and thereby, through Abel inversion, the estimation of the density structure [14].

In the absence of a gas jet, this work was focused on the characterization of a temperature profile around a welding iron. In this study, a Michelson interferometer [15] was assembled and, most relevant, an algorithm was developed in MATLAB for the reconstruction of the temperature distribution. In fact, realistic interferograms, where noise is present and where a non-uniform distributed parameter is usually being measured, rely on computer-based algorithms for their reconstruction. These methods are not free from certain assumptions along their steps, which might introduce significant errors and ultimately result in misleading values. Therefore, critical understanding and careful choice on the definition of such steps are of great importance through the data analysis process.

2. Experimental Setup

The experimental setup (see figure 1) consisted in a typical Michelson interferometer with a He-Ne laser. Here, the beam was divided in two equal parts by a cube beam splitter (BS), and those two beams were then reflected back by plane metallic mirrors (M) for their recombination. The welding iron was inserted in one of the interferometer arms, while the mirror of the other arm was tilted to better measure the shifted profile. A microscope objective (MO) and a lens with focal distance $f = 200$ mm (L1) were used to, respectively, expand and collimate the beam before the BS. A lens with distance $f = 50$ mm (L2) was used to focus the recombined beams at a CCD camera for image acquisition. The dimensions of the camera were 1928 x 1448 pixels, with a pixel size of 3.69 μm . Note that a polarizer (P) was placed to control the intensity going into the camera and a pinhole was used to spatially clean the beam coming from the laser. Several interferograms were acquired at room temperature (with the welding iron controller switched off) and at different temperatures. Interferograms with different number of lines were also acquired.

3. Phase extraction

The 2-D interferogram $I(x, y)$ may be described by

$$I(x, y) = B(x, y) + V(x, y)\cos[2\pi(\nu_0x + \omega_0y) + \phi(x, y)] \quad (1)$$

where ν_0 and ω_0 are, respectively, the fringe frequencies in the x and y directions, $\phi(x, y)$ is the required phase information, $B(x, y)$ describes variations in the background of the interferogram, and $V(x, y)$ describes variations in the fringe visibility [14]. In order to isolate the phase, we have to develop an algorithm with several steps [16, 17]:

1. read the acquired interferograms and perform a 2-D fast Fourier transform, from where three peaks appear at ω and $\omega \pm \omega_0$, given by

$$i(\nu, \omega) = b(\nu, \omega) + v'(\nu, \omega - \omega_0) + v'^*(\nu, \omega + \omega_0) \quad (2)$$

2. apply a 2-D filter in order to select one of the peaks around ω (in our case, the peak at $\omega - \omega_0$) and translate the filtered image to place this peak at ω ;
3. determine the logarithm of the 2-D inverse fast fourier transform which will give

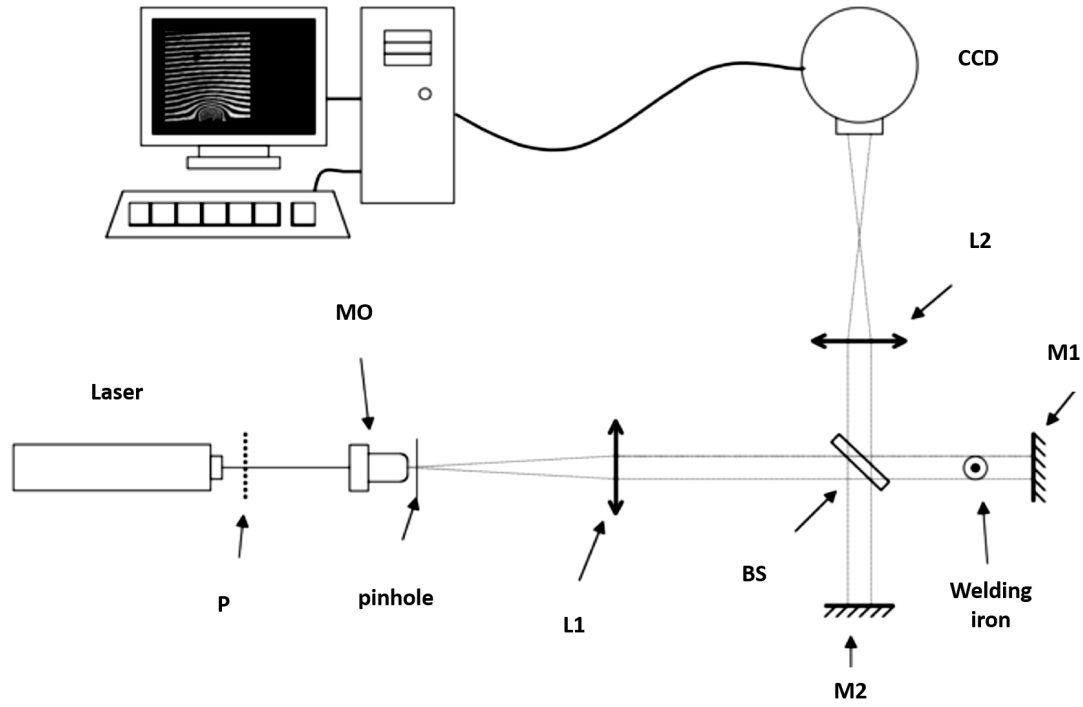


Figure 1: Experimental setup of a Michelson interferometer for the study of a temperature profile generated by a welding iron. Legend: P - polarizer; MO - microscope objective; L - lens; BS - beam splitter; M - plane metallic mirror; CCD - camera. (Image from *Óptica Coerente*, Protocolos de Laboratório LFEA, 2º Semestre 2016/2017)

$$\log[V'(x, y)] = \log[V(x, y)/2] + i\phi(x, y) \quad (3)$$

and isolate its imaginary part (this corresponds to a phase that is still undetermined by some factor of 2π);

4. unwrap the phase to obtain the true phase shift.

This steps need to be applied both for an interferogram with the perturbation in study and for a corresponding reference interferogram (without the perturbation). The determined unwrapped reference phase is then subtract to the unwrapped phase of the other interferogram, which should correct the latter one from any tilt and defects on the fringes.

4. Abel inversion

For the determination of the temperature distribution, one must apply the Abel inversion to determine the refractive index along the profile. Several methods have been proposed to overcome the main problems of the Abel inversion, which are the discontinuity at $x = r$ and the dependence on the first derivative of $\phi(x)$. Some of those methods are the discretization method, the Hankel-Fourier method and the Nestor-Olsen method [18]. Here, for simplicity, we use the discretization method which is based on the direct discretization of the Abel integral with a slight modification in the denominator to avoid the discontinuity. This method is applied on a $2N + 1$ data point discrete distribution of $\phi(x)$ with axial symmetry, and is given by

$$n(r_j) = -\frac{1}{2} \frac{\lambda_0}{2\pi^2} \sum_{i=j}^{N-1} \frac{\phi(x_{i+1}) - \phi(x_i)}{\sqrt{(x_i + \frac{\Delta x}{2})^2 - r_j^2}} + n_0 \quad (4)$$

where $n(r_j)$ is the refractive index in the radial direction r_j , λ_0 is the wavelength of the laser, Δx is the spatial separation between data (equal to the image resolution), x_i is equal to $i\Delta x$ with $i = -N, \dots, 0, \dots, N$, r_j is $j\Delta r$ with $j = 0, \dots, N$ (where, $\Delta r = \Delta x$) and n_0 is the reference refractive index (here, at 15 °C for $\lambda_0 = 631.8$ nm) [19]. The factor 1/2 was added to the equation once the beam crosses twice the profile. From the resulting profile, we can relate the refractive index with the temperature by [20]

$$T(r_j) = \frac{n_0 - 1}{n(r_j) - 1} T_0 \quad (5)$$

where $T(r_j)$ is the temperature in the radial direction r_j and T_0 is the reference temperature at 288.15 K (15 °C).

5. Results and discussion

An interferogram with approximately 10 fringes for the iron at 200°C and its correspondent reference interferogram at room temperature (see figure 2), were analyzed using MATLAB.

5.1. Phase extraction

The described method for the phase extraction was applied, where the selection of the finite filter and the phase unwrapping proved to be the biggest concern steps. Different sets of rectangular filters were tested and two of those are described and discussed below. See in figure 3, for better understanding, the 2D-FFT determined from the interferogram with the welding iron at 200 °C and the corresponding plot of the 2D-FFT signal for frequency $\nu = 0$, showing the three peaks. From those, we wanted to filter the peak that is on the negative side of $\omega = 0$. (Note that similar figures were obtained for the reference interferogram and therefore are not shown).

For the first set of filters, maximum horizontal and vertical dimensions were selected independently such that the resulting unwrapped phase of both interferograms was completely reconstructed (i.e. without any defects from the unwrap algorithm). This was only possible with the selection of a very small amount of frequencies in the vertical direction (ω):

- for the interferogram with the temperature profile the maximum horizontal and vertical dimensions of the filter were 230 x 3 pixels in the frequency domain,
- for the reference interferogram the maximum dimensions were 70 x 2 pixels.

Both phases were then subtracted, leading to the phase that can be seen in figure 4 (top). From here, we can state that although this amount of information seemed to be enough to reconstruct the profile around the cylindrical part of the iron, where maximum values between 2π and 2.5π could be expected from the raw interferogram, the same did not happen around its conical part. Furthermore, the subtraction of the phases selected by two distinct filters would lead to a non-homogeneous correction of the image, resulting in misleading values in the next step of the work (i.e, in the determination of the temperature values).

To overcome these problems, more pixels from the vertical direction had to be included in the filter and both images had to be equally filtered. To have enough information for the reconstruction around the conic shape, several tests showed that 11 pixels would be the optimum value to be selected from the vertical direction. However, the unwrapping algorithm function from MATLAB could no longer homogeneously reconstruct the phase in the right side of the iron. This can be seen for the second set of tested filters, with dimensions of 90 x 11 pixels, in figure 4 (bottom). A possible solution that could be tried in the future, would be to acquire interferograms with even more fringes. Also, a filter with a different shape could be alternatively tested.

Note that for both cases, after the correction of the phase, a mean of the surrounding part of the profile was performed in order to offset the phase data. This sets the region which corresponds to the place where the fringes are not changing, to approximately zero.

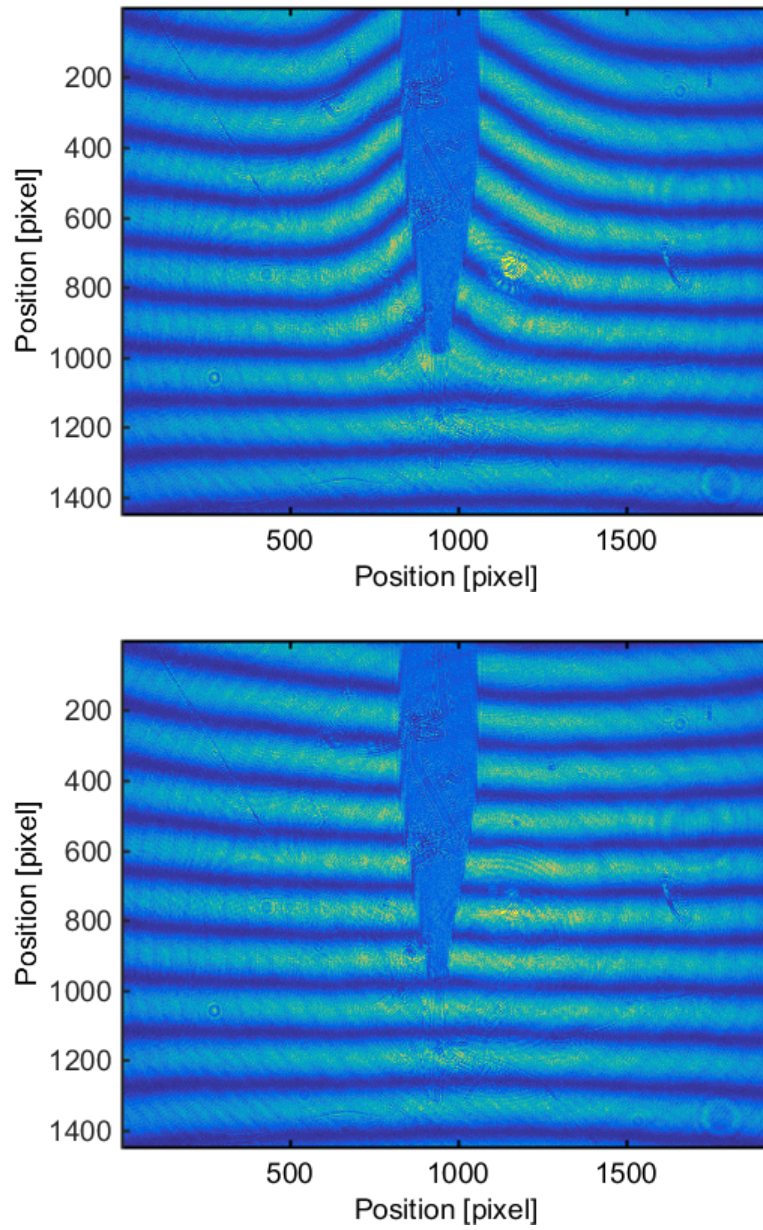


Figure 2: Top: Interferogram at 200 °C. Bottom: Reference interferogram (room temperature).

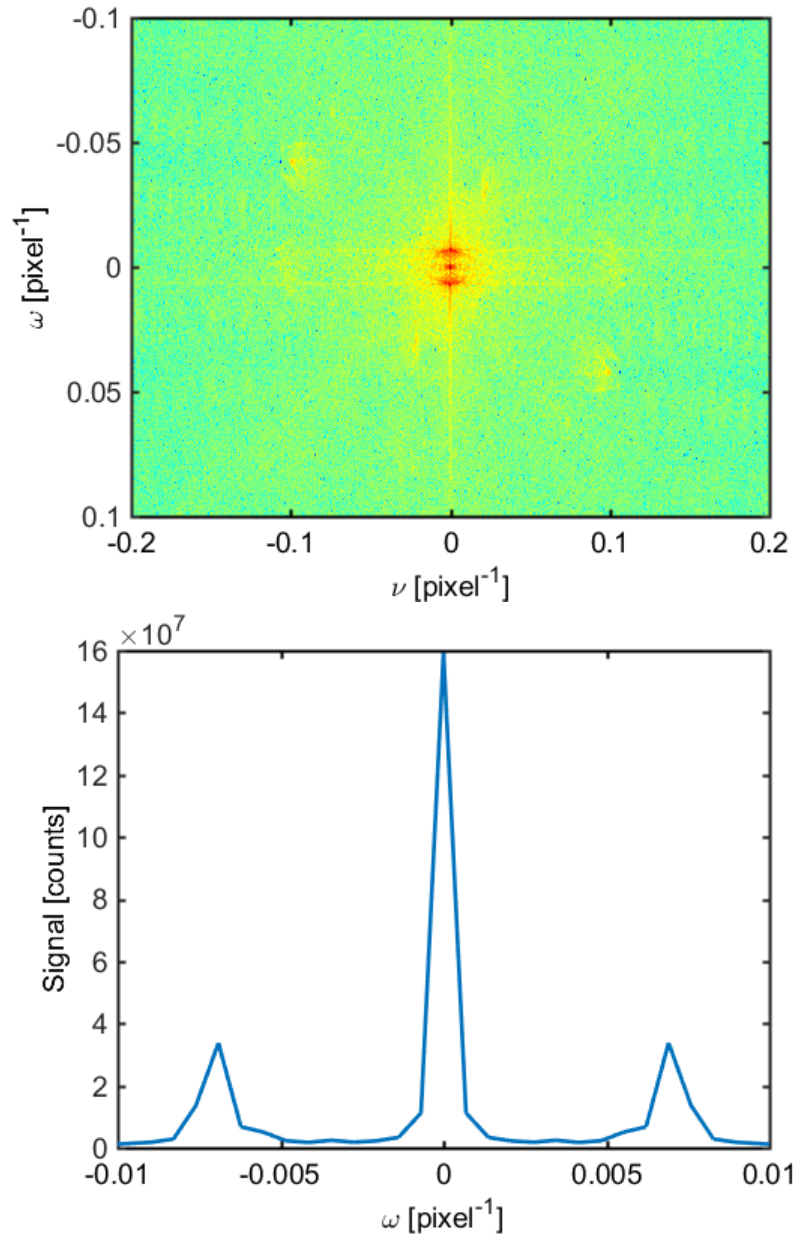


Figure 3: Top: Determined 2D-FFT of the interferogram at 200 °C (here, logarithm of the magnitude is presented only for better visualization). Bottom: Plot of the 2D-FFT signal for frequency $\nu = 0$ showing the three peaks.

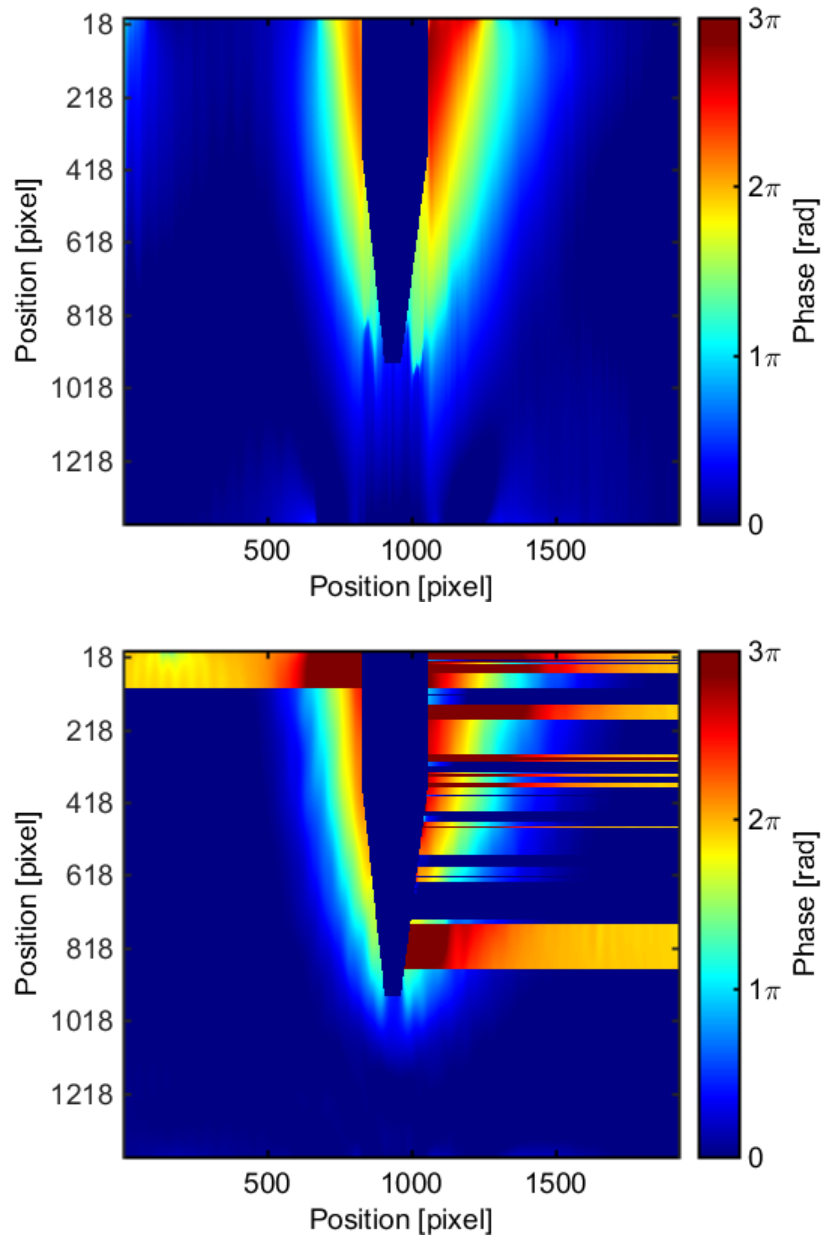


Figure 4: Top: Phase map of the interferogram for first set of filters (colour bar in radians). Bottom: Phase map of the interferogram for second set of filters (colour bar in radians).

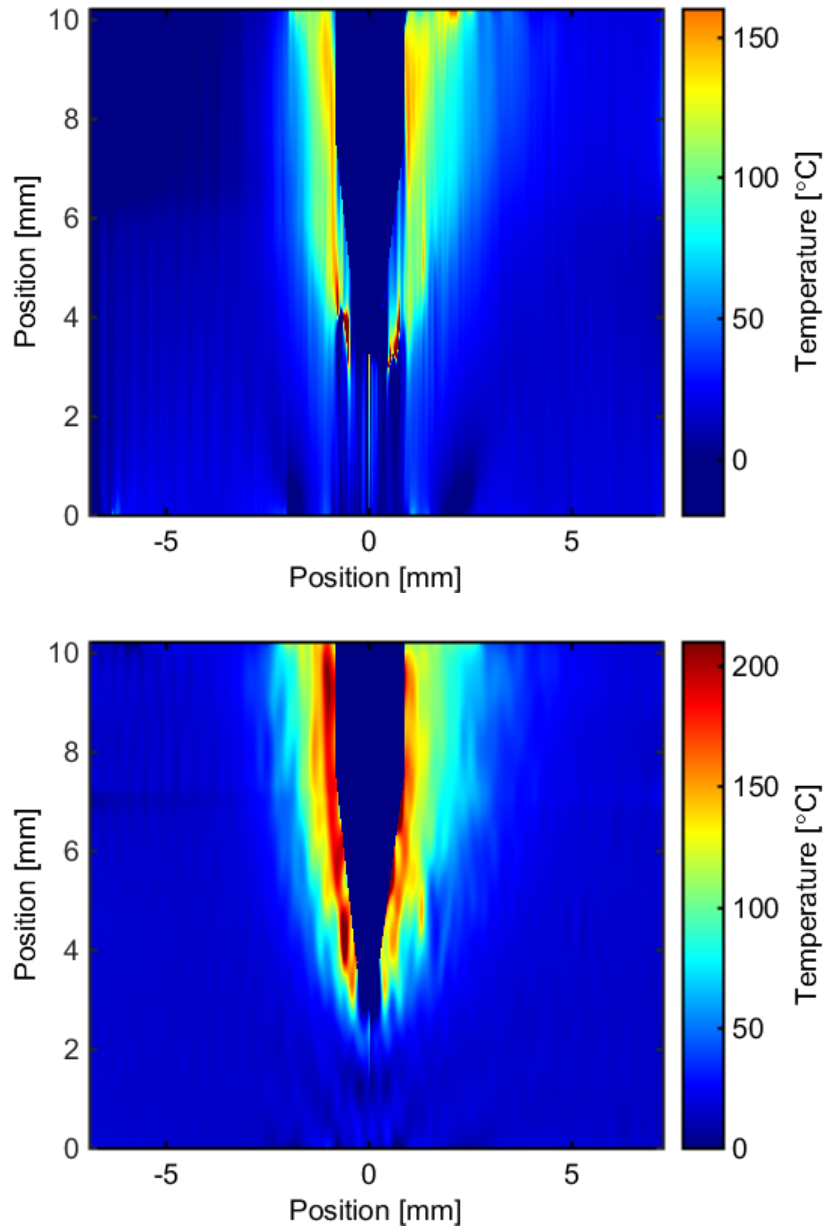


Figure 5: Top: Temperature profile for the first set of filters (colour bar in °C). Bottom: Temperature profile for second set of filters (colour bar in °C).

5.2. Abel inversion

The discretization method was then applied for both resulting phases. As this method assumes radial symmetry and the phase in analysis is clearly asymmetric, the integral was applied to both sides separately. Here, calibration of the pixel size and choice of the central axis were the most critical steps.

Indeed, the center of the data should correspond to the central axis of the iron. However, it was not clear from the images the exact pixels from where the iron starts and ends, so that its middle could be precisely determined. Furthermore, the iron is slightly tilted. From the top part of the row images the center was determined to be at approximately pixel number 945 and from the bottom at pixel number 938. Therefore, their mean (rounded to an integer) was calculated and considered as the center for the simulations.

Also, at this point, the pixel size needed to be calibrated to the real object size. This was done by measuring the top part of the iron with a calliper (1.70 ± 0.05 mm) and the correspondent size in pixels. The determined calibration was $7.33 \mu\text{m}/\text{pixel}$, correspondent to a magnification factor of 2. Note, that the reasons stated before also influence the precision of this calibration.

As expected, for the first phase, the determined temperatures do not correspond to realistic values, see figure 5 (top). Indeed, although the maximum temperature achieved was ~ 200 °C, it stabilizes at different values at each end side of the image. Also, it is clear that the temperature gradient around the conical part could not be reconstructed.

For the second set of filters, however, the temperature profile could be reconstructed with realistic values, see figure 5 (bottom). Indeed, although the calculated phase had jumps in the values at the right side of the iron, this was just affecting the vertical direction. Thus, when performing the phase difference between columns of the image (as required by the discrete method), these jumps have no negative impact on the calculations of the refractive index. The resulting profile is smoothly reconstructed along all the iron with two different maximum values on each side (one of ~ 200 °C and the other of ~ 155 °C). This difference is consistent with the fact that the fringes do a different shift for both sides. At the edges, the same temperature of 15 °C was determined, consistent with the used reference temperature.

At this stage, other horizontal dimensions for the filter were tested. Dimensions higher than 90 pixels led to a less homogeneous temperature profile. Dimensions lower than 90 led to a lack of information for the reconstruction of the temperature profile. This proved that the second set of filters (90 x 11 pixels) was the closest to the optimal one for the data in case (considering the rectangular shape).

In the future, precise measuring of the room temperature should be performed. Also tests in better isolated environment should be done allowing the measurement of a more symmetric profile with maximums closer to each other.

6. Conclusions

Experimental work and numerical analysis using laser interferometry for characterization of a temperature profile were presented.

The influence on the dimensions of the filters used to extract the phase was studied. Two set of filters were discussed. From the first set of filters, phase profile could be determined without noise but the selected amount of information did not allow for the realistic reconstruction of the phase around the conic shape of the iron. From the second set of filters (with larger vertical dimension on the Fourier frequency domain), the unwrap algorithm could not extract correctly the phase at the right side of the iron. However, as this problem was only affecting the vertical direction, it did not affect the final results.

Maximum phase shift was determined to be between 2π and 2.5π and maximum temperature to be approximately 200 °C. This is in accordance with the interferogram and the temperature that was set in the controller of the iron.

In general, this work allowed me to get familiar and aware of the important role that this optical diagnostic tool plays in many fields and how careful its data must be analyzed.

In the future, interferograms with more lines should be acquired in a more isolated environment, to overcome the difficult reconstruction around the conical shape of the iron and to avoid the measurement of a non-symmetric profile. Also, different filter shapes should be tested for the phase reconstruction.

References

- [9] S. M. Hooker. ‘Developments in laser-driven plasma accelerators’. In: *Nat. Photonics* 7 (10 2013), 775–782.
- [10] T. Brabec and F. Krausz. ‘Intense few-cycle laser fields: Frontiers of nonlinear optics’. In: *Rev. Mod. Phys.* 72 (2 2000), 545–591.
- [11] D. P. Umstadter. ‘All-laser-driven Thomson X-ray sources’. In: *Contemp. Phys.* 56 (4 2015), 417–431.
- [12] N. Lemos *et al.* ‘Guiding of laser pulses in plasma waveguides created by linearly-polarized femtosecond laser pulses’. In: *Sci. Rep.* 8 (1 2018), p. 3165.
- [13] J. Peiyong. ‘Photon acceleration based on plasma’. In: *Phys. Rev. E.* 64 (3 2001), p. 036501.
- [14] K. Nugent. ‘Interferogram analysis using an accurate fully automatic algorithm’. In: *Appl. Opt.* 24 (18 1985), pp. 3101–3105.
- [15] W. Lauterborn and T. Kurz. *Coherent Optics*. Berlin: Springer, 2003.
- [16] M. Takeda *et al.* ‘Fourier-transform method of fringe-pattern analysis for computer-based topography and interferometry’. In: *J. Opt. Soc. Am.* 72 (1 1982), pp. 156–160.
- [17] N. Lemos. ‘Characterization of ionization fronts by interferometric diagnostics’. MSc Thesis. Lisbon: Instituto Superior Técnico, 2007.
- [18] R. Álvarez *et al.* ‘An Abel inversion method for radially resolved measurements in the axial injection torch’. In: *Spectrochimica Acta Part B* 57 (11 2002), pp. 1665–1680.
- [19] P. E. Ciddor. ‘Refractive index of air: new equations for the visible and near infrared’. In: *Appl. Optics* 35 (9 1996), pp. 1566–1573.
- [20] K. J. Gåsvik. *Optical Metrology*. Chichester: John Wiley & Sons, 2002.

Optimization of High Harmonic Generation in Gases



Mukhtar Hussain originates from countryside of Pakistan. Prior to join APPLAuSE PhD program, he was an Early Stage Researcher in the Single Cycle Laser (SYLOS) Group of the Laser Infrastructure Division at Extreme Light Infrastructure - Attosecond Light Pulse Source (ELI-ALPS), Szeged Hungary. Where, his tasks and responsibilities covered beam distortion characterization for a new design of thermal lens compensation in a Ti:S-based preamplifier system and experimental preparation of a pump-probe setup based on transient diffraction method.

He did his MS Physics from COMSATS Institute of Information Technology, Lahore, Pakistan and MSc in Computational Physics from Center of High Energy Physics (CHEP), University of the Punjab. He worked as a Lecturer in University of Management and Technology (UMT) and at Govt. College University Faisalabad (GCUF), Sahiwal Campus for one year, alternately. He also worked as research assistant in Lahore University of Management Sciences (LUMS), Lahore, Pakistan and King Saud University (KSU) Riyadh, Saudi Arabia.

Mukhtar Hussain

GoLP/Instituto de Plasmas e Fusão Nuclear (IPFN), Instituto Superior Técnico, Avenida Rovisco Pais, 1049-001 Lisboa, Portugal

E-mail: mukhtar.hussain@tecnico.ulisboa.pt

February 2018

Abstract.

In this work, we will generate and optimize high harmonic generation in a gas cell by using various gases: Ar, Xe and Ne. The high harmonic generation are generated by using an ultrafast high average power laser (coherent Astrella) with a central wavelength of 800 nm, operating at 1 kHz, pulse duration 45 fs and energy of 7.5 mJ. The optimum intensity (10^{14} W/cm²) of the incident pulses are obtained by focusing the pulses into a 10 mm diameter and 15 mm long gas cell by employing the 750 mm focal length focusing lens. The intensity profile (foot prints) of the high harmonics is recorded by installing the XUV-CCD (Princeton Instruments PIXIS-XO 1024B) camera. The optimization of the high harmonic generation in Ar, Xe and Ne is performed by pressure scan, focusing position scan in gas cell, incident beam diameter variation and with various thickness Al filter. The stability of the optimized high harmonic generation in Ar, Xe are recorded by shot to shot variation analysis. Furthermore, the high harmonics are generated in Ar by collinearly focusing the fundamental and second harmonic i.e. (800 & 400) nm in a gas cell and observe the signature of even order harmonics in Ar. The rotational effect of BBO on the high harmonic in Ar are also investigated.

1. Introduction

High harmonic generation (HHG) is a non-linear process in which the laser light of certain intensity is focused on a target (gas, plasma or solid), as a result the harmonics of odd or even and odd harmonic frequencies of the incident laser are emitted. In 1977, the first HHG was observed by the interaction of CO₂ laser with the plasma generated solid targets [21]. The HHG in gases was first generated by the McPherson and colleagues in 1987 [22]. The HH intensity decreased at low orders, then form a plateau where the intensity of the harmonic remains constant over many orders [23]. The harmonics of the plateau spanning over hundreds of the eV measured that extended to the soft X-ray [24].

In the spectrum of HHG the plateau ends up at position abruptly known as HH cut off. The harmonic cut off varies linearly with the increase of laser incident intensity till the saturation intensity is reached [25]. By replacing the atomic species with lighter noble gases, the saturation intensity can be increased but they have the lower conversion efficiency. So, for higher brilliance a balance required to be instituted between the saturation intensity and the target nature depending upon the photon energies required.

HHG depends upon the spatio and temporal profiles of the driving laser field, therefore the harmonics have similar temporal and spatial coherence properties [26]. The pulse durations of the HH is often shorter than the driving laser pulse durations, which is due to the non-linear processes such as ionization and phase matching. The harmonics are produced oftenly in a small temporal window, when the phase matching condition is attained. It was demonstrated that the high harmonic generation due to the ionization of the generating media is attributable to the leading edge of the driving pulse [27].

The analytical description of the HHG in gases can be retrieved with the “Three Step Model” which was developed by P B Corkum [28]. The three-step model can only describe the dynamics of one electron in HHG and the maximum producible photon energy, which is emitted on the recombination of electron with the parent ions. This model describes also how the laser parameter can affect the HHG via the pondermotive force but unable to explain the characteristic spectrum of the HHG. For the spectrum, the quantum mechanical approach must be used, which was first described by the Lewenstein [29]. For the optimization of macroscopic of HH signal to obtain the at least half of the maximum possible output signal, the following conditions need to be fulfilled [30]; $L_{med} > 3L_{abs}$ and $L_C > 5L_{abs}$.

HHG has many interesting properties. HHG is a robust mechanism to generate the XUV/soft X-rays in table top setup. The optical properties of XFEL heated matter was investigated with high order harmonics and showed temperature dependent electronic structure in warm dense matter [31]. An XUV pump–XUV probe experiment, which examines the dynamics of a thin-metal layer structure exposed to high-intensity XUV excitation is reported in [32].

In this lab rotation, the HHG in Ar, Xe and Ne by using an ultrafast high average power laser (coherent Astrella) with a central wavelength of 800 nm, operating at 1 kHz, pulse duration 45 fs and energy of 7.5 nJ are reported here. The optimization of the HHG in Ar, Xe and Ne is carried out by pressure scan, focusing position scan in the gas cell, incident beam diameter variation and using various thickness Al filter. The stability of the optimized HHG in Ar, Xe are recorded by the shot to shot variation analysis. Furthermore, the rotational effect of BBO on the high harmonic in Ar are investigated.

The objective of this lab rotation was to optimize the HHG in noble gases and proposed the benchmark for the future experiments at the VOXEL lab correlated to HHG. The optimized HH can be used to probe the warm dense matter (WDM) to explore the ultrafast dynamics.

This report is structured as: the experimental setup for the generation of HH and optimization is described, primarily. The optimized conditions for high harmonic generation, spectral measurements of HH, the pressure scan, shot to shot stability of HH in Ar and Xe; finally, the rotational effect of BBO on the intensity of HH in Ar is described in results and discussion section.

2. Experimental setup and optimization of HHG

The schematic of the HHG, foot-print measurements and spectrometer setup for spectral components measurements is shown in figure 1. The output of the Astrella laser system (7.5 mJ) is sent to 50:50 beam splitter to use only the

reflected part, energy is controlled by using two irises and is focused in the rear edge of gas cell having dimension of 10 mm diameter and 15 mm long. The Al filter of 464.5 nm thickness of 28.5% calibrated transmission is inserted to block the near-IR pulses and the HH are directed to the XUV-CCD camera by a flat mirror. The foot-print of the HH is measured and optimized as shown in the inset figure 1.

The HHG pulses in gas cell are filtered by 464.5 nm and 150 nm Al filter one by one and together as well. The HH signal after the Al filter are incident at grazing angle (9°) on spherical mirror with a radius of curvature of 10 m. The focused HH pulses are directed to a grating (1000 lines/mm), which resolves the signal into its spectral components by an Au coated flat mirror. The distance between the grating and the XUV-CCD (Princeton Instruments PIXIS-XO 1024B) is kept of 36 cm. The resolved spectral components of HH pulses are imaged on the XUV-CCD, as shown in inset of figure 1.

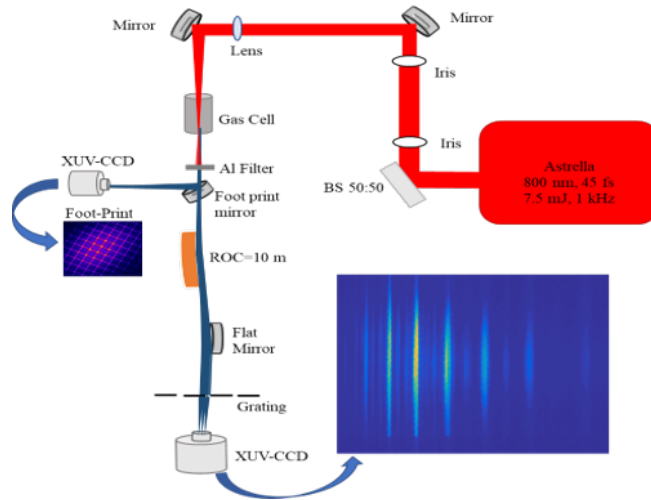


Figure 1: Schematic of HHG, foot-print measurements, and Spectrometer setup for the measurement of HHG in gases at the VOXEL lab. The foot print mirror is flipped only at the foot print (intensity profile) measurements.

3. Results and Discussions

3.1. Optimized conditions for high harmonic generation

The HHG is optimized in Ar, by adjusting focusing position of incident laser pulses in the gas cell, pressure scan from 2 mbar to 20 mbar in gas cell, iris aperture scan, different Al filter thickness and their combination are calibrated. The incident laser focus is kept at the exit of the gas cell for optimized HHG. The HHG pulses in gas cell are filtered by 464.5 nm Al filter. The optimized conditions which obtained from recording the foot-print of HHG in Ar, Ar @ (400 & 800) nm, Xe and Ne gases at gain 3 of CCD which corresponds to one electron per count are listed in table 1. The energy of HH in Ar @ (400 & 800) nm, Xe and Ne are calculated from the spectrometer calibration counts.

Gas	P(mbar)	Aperture size(mm)	HH Photon No.	HHE (nJ)
Ar	13.5	8	6.94E+07	2.34
Ar*	7.5	11	4.54E+07	1.53
Xe	3.5	8	6.27E+07	2.12
Ne	15	8	5.97E+05	0.02

Table 1: The optimized conditions for high harmonic generation in Ar, Ar* @ (400 & 800) nm, Xe and Ne

3.2. Spectral measurements of high harmonics

The spectrum of HHG in Ar, Xe and Ne under the optimized conditions as listed in table 1 is measured by using the XUV spectrometer. The HHG in Ar are generated by collinearly focusing the fundamental pulses (800 nm) and second harmonic (400 nm) which are generated in 100 μm thick BBO crystal. Odd harmonics are ascribed to the fundamental (800 nm) and even harmonic are attributable to the second harmonic (400nm) pulses focused to the Ar gas in the gas cell. The HH21, HH23, HH25 and HH27 have a higher brilliance when high harmonics are generated from only near IR (800 nm) and HH25 is the dominant one) as shown in the figure 2a, while the HH17, HH19, HH21 and HH23 have higher photon number when generated by fundamental pulses (800 nm) and its second harmonic pulses (400 nm). The HH21 is dominant in the HH spectrum as shown in the figure 2b.

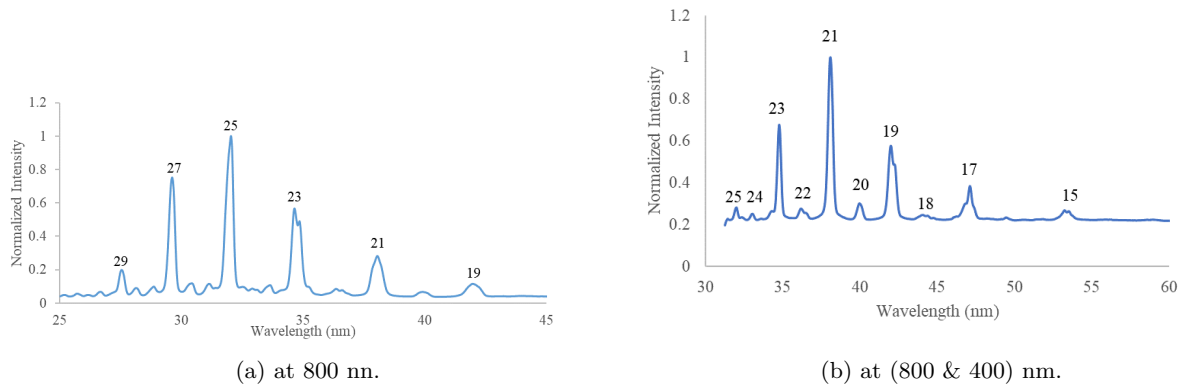


Figure 2: High harmonic spectrum normalized to the strongest HH order.

The shifting of peaks and generation of relatively lower order harmonics in Ar when pumped by fundamental and its second harmonic pulses ascribed to lower energy of the focused incident pulses into the gas cell, attributable to the lower conversion efficiency of BBO crystal. Furthermore, the contribution from the long trajectories results in a small HH signal, because they lead to a short coherence length L_c compared to the short trajectories. The high harmonic spectrum in Xe and Ne under the optimized conditions is shown in figures 3a and 3b, respectively. The HH19 and HH37 are dominant in Xe and Ne generated high harmonics, respectively. The energy of the harmonics calculated from the spectrometer is 5.44 times smaller than that the CCD measurements. The throughput of our spectrometer is 18.4%.

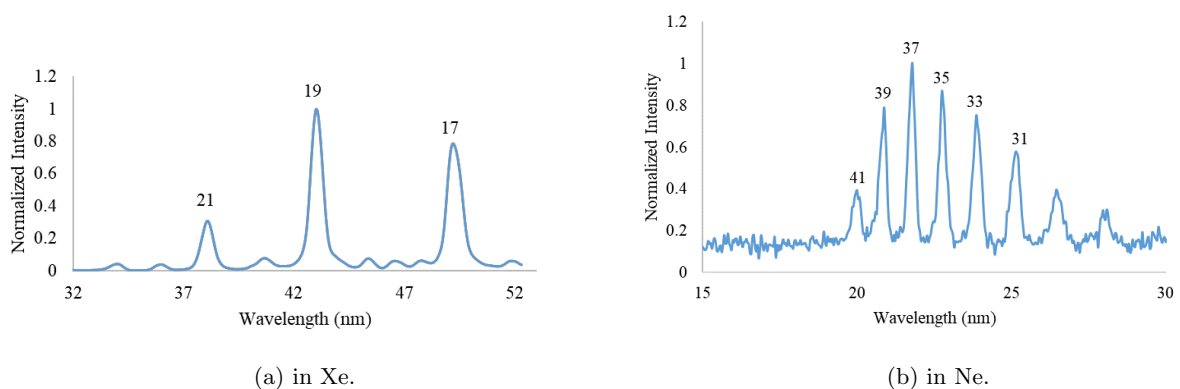


Figure 3: High harmonic spectrum normalized to the strongest HH order.

3.3. Pressure and stability scan of high harmonics in Ar and Xe

The high harmonic intensity of Ar and Xe for each HH order is recorded by using the spectrometer setup for different gas cell pressure under the fixed experimental conditions such as pulse energy, beam diameter, focusing

lens position and focusing position of the laser pulses in gas cell. The behavior of normalized integrated photon number variation with different gas cell pressure for Ar (figure 4a) and Xe (figure 4b). At higher pressure in the gas cell the intensity of the HH are low which attributable to mainly phase matching conditions are not fulfilled. The other factor of lower intensity is due to the inefficiency of the vacuum system to extract leaked Ar and Xe gases from the gas cell.

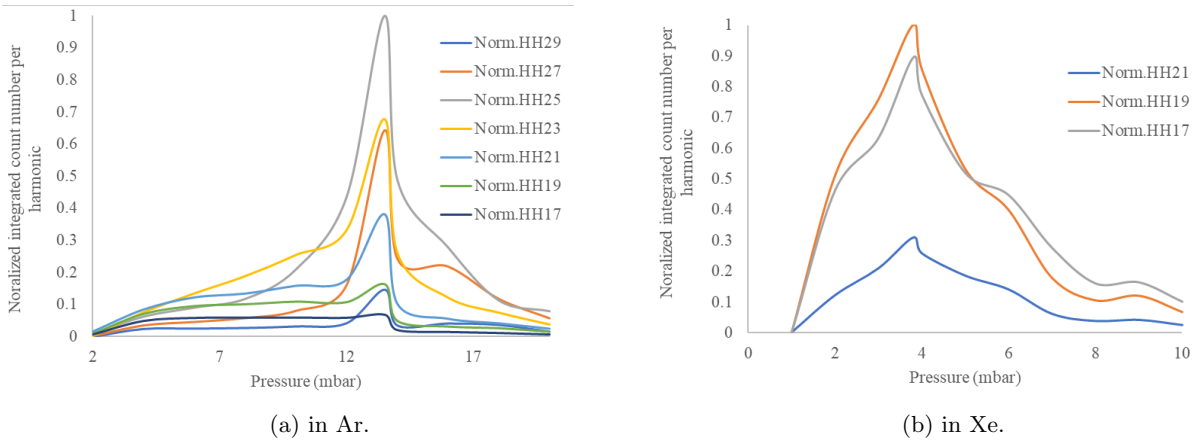


Figure 4: Pressure scan of the integrated signal per HH order.

The HH beam stability is important in terms of wave front and intensity from shot to shot to confirm the repeatability. The intensity stability of high harmonic generation in Ar under optimized pressure (13.5 mbar) and in Xe (@ 8 mbar) is recorded for the integration time of 50 ms shown in the figures 5a and 5b. The different HH orders exhibit the collective behavior of rise and fall in intensity at certain time step for Ar and Xe. Such behavior might be ascribed to the incident laser intensity fluctuations which affect the HHG process. The fluctuations in shot to shot is smaller for lower order HHs while its higher for the high HH orders. This results smaller standard deviation for HH orders with longer wavelength. The variation in integrated count number per harmonics from shot to shot have the approximate same pattern as shown in the figure 5.

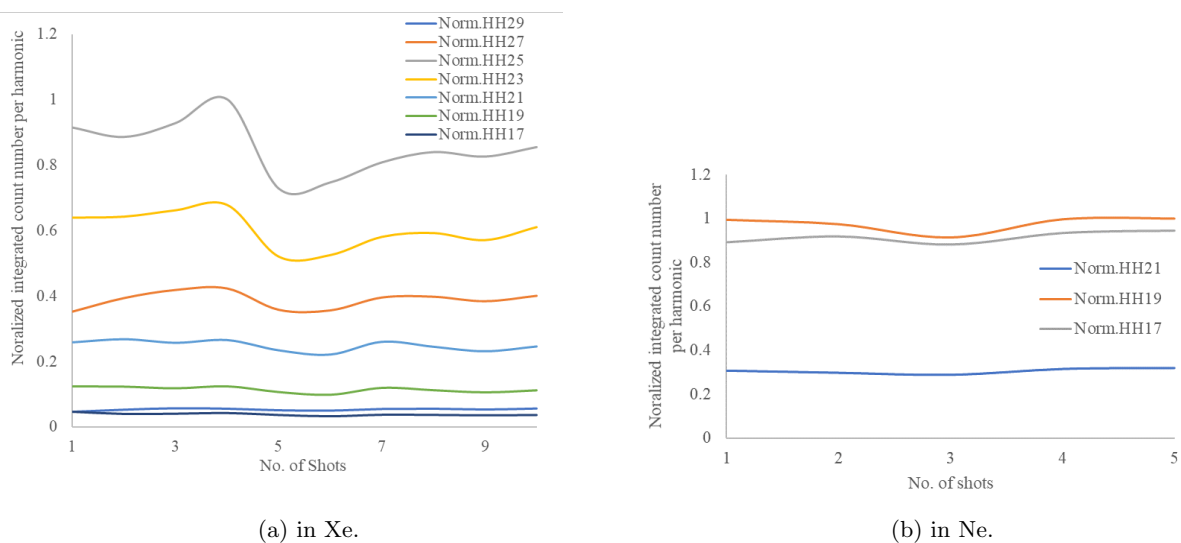


Figure 5: Shot to shot stability of HHG.

3.4. Rotational effect of BBO on high harmonics in Ar

To record the effect of second harmonic collinearly with the fundamental incident laser pulses on the high harmonic generation phenomena in Ar, a 100 μm BBO used to generate the second harmonic (400 nm) is focused on the Ar filled gas cell. The effect of the BBO rotation on the relative normalized count number at the optimized condition is investigated, as shown in figure 6. The maximum number of photons or intensity of each harmonic order is observed at '0' position of BBO in the rotational mount and falls as rotate further either in clock wise or anticlockwise.

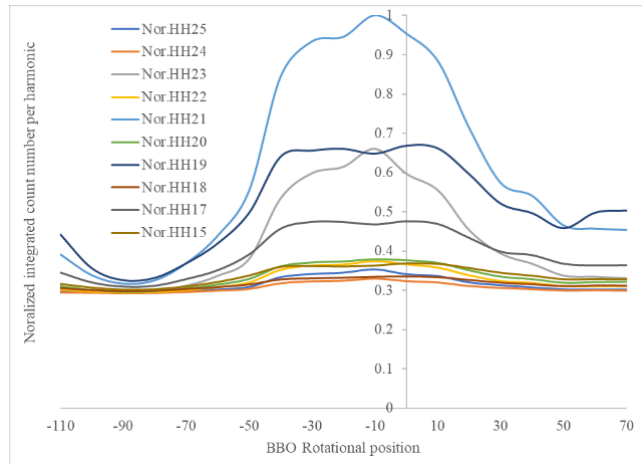


Figure 6: The Variation of integrated signal per HH order as a function of BBO rotation in Ar.

In this work, we have generated high harmonics in Ar, Xe and Ne by focusing the 800 nm, 1 kHz, 45 fs pulses in a 15 mm long gas cell. We also observed high harmonics in Ar by focusing fundamental and second harmonic pulse in gas cell. The foot-print of the high harmonics is recorded and optimized by employing the XUV-CCD (Princeton Instruments PIXIS-XO 1024B). The optimization of the high harmonics is carried by changing the focusing geometry, focusing position in the gas cell, incident laser beam diameter, and at different pressure in the gas cell. The XUV spectrometer is setup to record the spectrally resolved HH orders in spectrum of Ar, Xe and Ne gases. The effect of BBO rotation on the high harmonic orders is investigated, which shows the intensity dependence of high harmonic orders on it. The shot to shot stability of HHG in Ar and Xe shows that the instability is higher at the high order harmonics.

References

- [21] Burnett N H et al. 'Harmonic generation in CO₂ laser target interaction'. In: *Appl. Phys. Lett.* 31 (172-174 1977).
- [22] McPherson A et al. 'Studies of multiphoton production of vacuum-ultraviolet radiation in the rare gases'. In: *JSOA B.* 4 (595 1987).
- [23] Li X F et al. 'Multiple-harmonic generation in rare gases at high laser intensity'. In: *Physical Review A.* 39 (5751-5761 1989).
- [24] Seres J et al. 'Laser technology: Source of coherent kiloelectronvolt X-rays'. In: *Nature* 433 (596 2005).
- [25] Brabec T and Krausz F. 'Intense few-cycle laser fields: Frontiers of nonlinear optics'. In: *Reviews of Modern Physics* 72 (545-591 2000).
- [26] L'Huillier A, Schafer K J and Kulander K C. 'Theoretical aspects of intense field harmonic generation'. In: *Journal of Physics B: Atomic, Molecular and Optical Physics* 24 (3315-3341 1991).
- [27] Schafer K J and Kulander K C. 'High Harmonic Generation from Ultrafast Pump Lasers'. In: *Physical Review Letters* 78 (638-641 1997).

- [28] Corkum P B. ‘Plasma perspective on strong field multiphoton ionization’. In: *Physical Review Letters* 71 (1994-1997 1993).
- [29] M. Lewenstein et al. ‘Theory of high-harmonic generation by low-frequency laser fields’. In: *Physical Review A* 49.3 (2117 1994).
- [30] E. Constant et al. ‘Optimizing high harmonic generation in absorbing gases: Model and experiment’. In: *Physical Review Letters* 82.8 (1668 1999).
- [31] Gareth O. Williams et al. ‘Tracking the ultrafast XUV optical properties of x-ray free-electron-laser heated matter with high-order harmonics’. In: *Physical Review A* 97 (023414 2018).
- [32] Allaria E et al. ‘Two-colour pump-probe experiments with a twin-pulse-seed extreme ultraviolet free-electron laser’. In: *Nature Communications* 4 (2476 2013).

Synthesis of graphene sheets produced in a microwave plasma reactor



Ruggero studied Engineering Physics at Politecnico di Milano where he obtained both bachelor and master degrees. In his career he has been committed in different topics. The courses he attended at Politecnico di Milano covered a wide range of subjects from those physics related, as quantum physics and optics, to those more engineering oriented such as electronics, informatics, and control theory.

During his bachelor he dealt with ultrathin films and he graduated with a thesis titled *Growth studies of metastable Co on Fe(001) and on Fe(001)-p(1x1)O*. He carried out his master thesis at European Synchrotron Radiation Facility (ESRF) in France where he worked on temperature measurements at megabar pressures.

Before joining the APPLAuSE program at IPFN he has spent several months working both at ESRF and at Diamond Light Source (DLS) at the Harwell Science and Innovation Campus, England. There he gained valuable experience in working in a cooperative, stimulating and international environment and he took part in many x-ray absorption spectroscopy (XAS) and x-ray diffraction (XRD) experiments.

He thinks that a broad and solid basic preparation is of vital importance for a scientist and he strives to keep raising his knowledge and competences. Currently, he is interested in Quantum Fluids of Light and he joined the Ultra Cold Plasma group at IPFN to carry out his PhD thesis.

Ruggero Giampaoli

Instituto de Plasmas e Fusão Nuclear (IPFN), Instituto Superior Técnico, Avenida Rovisco Pais, 1049-001 Lisboa, Portugal

E-mail: ruggero.giampaoli@tecnico.ulisboa.pt

February 2018

Abstract.

During the lab rotation that has been carried out at the Plasma Engineering Laboratory (PEL) of N-PRiMe group at IPFN we have taken part in many experiments concerning both synthesis and analysis of graphene sheets. In this report we attempt to summarise the main results we obtained. Optical emission spectroscopy was performed on pure Ar plasma and on a Ar-CH₄ plasma at atmospheric pressure in order to analyse the atomic species excited by the plasma. Also, we have carried out scanning electron microscopy (SEM) measurements to analyse and compare the morphological structure of graphene produced in different thermodynamic conditions. Plasma temperature has been measured using the Boltzmann plot technique applied to the OH-rotational emission spectrum.

1. Introduction

In recent years, due to their electrical, mechanical, optical and chemical properties, graphene and doped graphene nanostructures have become more and more important and have drawn the interest of both academia and industry. The number of potential applications of graphene is really huge and ranges from optoelectronic to bio-engineering. Lately, increasing attention has been paid to heteroatoms doped graphene [33]. In particular, N doped graphene seems to be a promising material as electrode in batteries and supercapacitors [34], providing at the same time large capacity and high charge-discharge rate. Graphene quantum dots (GQD), small graphene fragments of a size less than 20-30 nm [35] with pronounced quantum confinement effects, show interesting photoelectric properties [36] which, coupled with low toxicity, high solubility in various solvent and carbon abundant availability, make GQD much more desirable for many applications compared with inorganic semiconductors quantum dots.

Graphene is made of sp^2 hybridized carbon atoms arranged in a two-dimensional hexagonal crystal lattice and its performances crucially depend on its structural characteristics [37] (e.g. defects, distribution of impurities, number of monolayers, presence of sp^3 carbons etc) and, therefore, on its fabrication method [38]. The reported methods for graphene synthesis can be divided into 'top-down' or 'bottom-up' approaches. Two examples of the 'top-down' strategy are the mechanical exfoliation of highly oriented pyrolytic graphite and the thermal reduction of graphene oxide. Bottom-up approaches include epitaxial growth and chemical vapour deposition. Nevertheless, a method that has been proved to be promising for an efficient large scale production of graphene derivatives is the microwave plasma-based process [37, 38].

Therefore, in the Plasma Engineering Laboratory (PEL), pristine graphene and N doped graphene are being produced using microwave plasma-based methods [38, 39, 40]. For highly oriented pristine graphene synthesis Ar and a carbon based precursor are injected in a quartz tube at atmospheric pressure and plasma is generated and sustained in the tube by microwave surface waves. In this type of reactor, plasma electrons dissociate the precursor and play a catalytic role for the growth of several carbon allotropes. The main advantage of this technique is that, since the plasma provides both an highly reactive environment that causes the precursor dissociation and the thermodynamic conditions that allow nanostructure assembling, there is no need to add catalysts in the system [41]. This results in a less toxic environment and in highly stable and reproducible processes [37]. Furthermore, microwave discharge based reactors are electrodeless: even if large power densities are injected in the reactor there is no electrode that has to be regularly replaced after being damaged by the plasma. Therefore, microwave based reactors, which can work as continuous-flow systems and can manufacture high quality graphene in a reproducible and clean manner, are very promising for low-price large-scale fabrication of graphene. To achieve this goal is very important to investigate the strong correlations between the plasma features and material properties. Thermodynamic properties of the plasma should be carefully tailored to obtain a high yield of graphene with the desired characteristics [42].

2. Synthesis of pure graphene: setup description

Since the main objective of PEL is to optimize the production of graphene and its derivatives at large scale, along with the PEL team I have been involved in the commissioning of a microwave plasma torch developed for that purpose. This setup is close to the one described in [37, 41, 42, 43, 44]; Fig.1 provides a simplified schematic of the setup. A magnetron, controlled by a high voltage generator, produces microwaves at 2.45 GHz. The output of the magnetron is connected to a circulator which shields the generator by absorbing the reflected power coming back from the line. Beyond the circulator, microwaves propagate in a rectangular metallic waveguide coupled with a surfatron: this device is a surface wave launcher that creates a wave propagating along the interface between the plasma and the quartz tube surrounding it. In other words, the surfatron [44][45] transform the electromagnetic mode propagating in the waveguide (TE_{10} with the electric field parallel to the quartz tube) into a surface wave propagating in the quartz tube attached perpendicularly to the waveguide. Surface waves sustain the plasma that can thus propagate outside the metallic waveguide into the quartz tube. The system allows to tune the impedance of the line in order to reduce at the minimum the reflected wave and to assure high power in the centre of the quartz tube. This tube has been specifically designed in order to foster graphene production [38]: the cylindrical tube has an expanding radius that promotes the departure from the supersaturation condition and therefore the growth of those carbon nanoparticles that have already reached the critical size for graphene nucleation rather than promoting

the nucleation of new nanostructures. Moreover, this tube configuration gradually reduces the flow velocity, thus increasing the precursor particle dwelling time in the plasma and, consequently, the time in which plasma acts as a catalyst for the starting precursor dissociation processes and for the nanoparticle assembling phase[41].

Both Ar and precursor fluxes are precisely regulated by means of a MKS247 controller connected to flux meters. The plasma is generated downwards and the graphene particles are collected in three different containers. To enhance the graphene sheets yield a tornado type Hurricane Cyclone System [38] has been used to gather particles in the second container. The exhausted products are then forced to flow in a fourth vessel filled with water in order to collect those particles that couldn't be captured before.

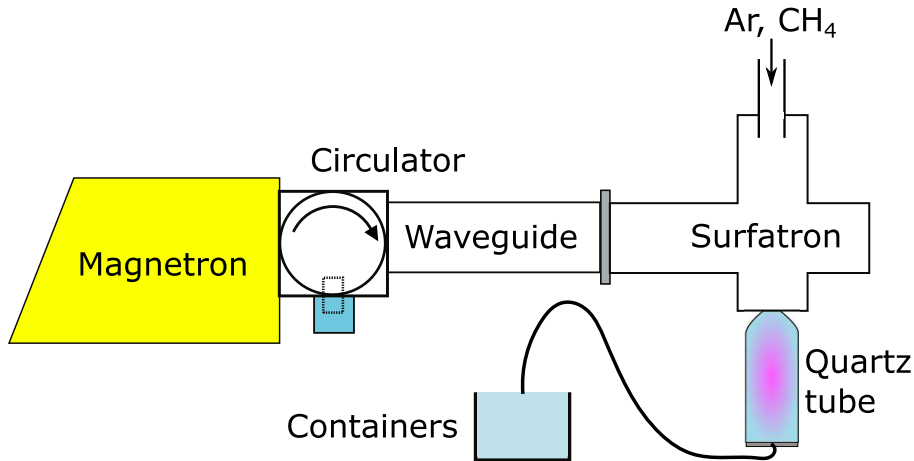


Figure 1: Schematic representation of the microwave plasma setup used during the lab rotation to produce graphene.

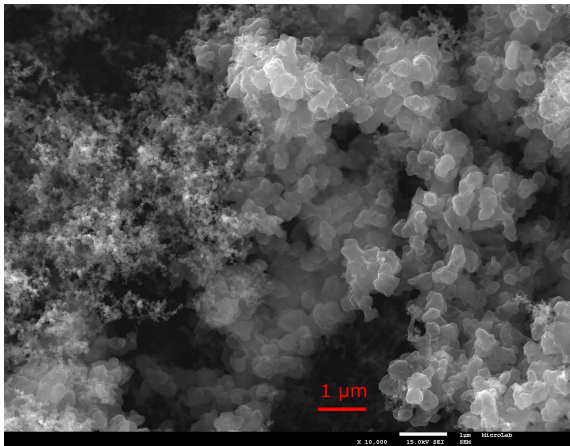
3. Results and discussion

3.1. Material characterisation

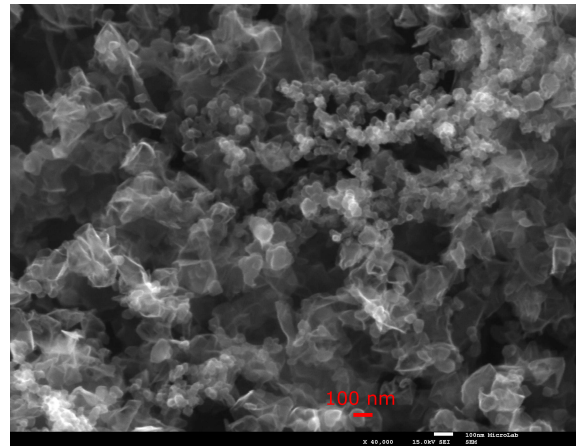
Several experiments have been performed using methane as precursor. We have set the Ar flux at 1200 sccm and the generator power at 2 KW. The experiment has been repeated several times changing in each run the methane flow. At the end of each run, graphene particles have been collected from all the four containers and separately analysed with a Scanning Electron Microscope (SEM). The goal of this analysis is to monitor the reactor output in order to optimise both the setup and the synthesis procedure to increase the graphene production yield over other morphologies. Here we present a preliminary analysis of the samples we have collected; in particular, in Fig.2 we show some of the different carbon morphologies we have observed so far. In Fig.2a tile and cluster particle like structures are shown. The tiles in the first structure are made of carbon nanosheets: one or few layers graphene is likely to be found here. Fig.2b shows the typical curl/wavy morphology of graphene sheets mixed with particle like morphologies. It is worthy noticing that Fig.2a and Fig.2b have different scales; therefore, the sheet like and particle like structures can be observed mixed in different proportions and at different scales. Moreover, even the dimensions of these structures can have a wide range of sizes: for instance, Fig.2c shows a structure which has the morphological characteristics of graphene with a quite large surface ($\approx 0.2 \mu m^2$) compared to the surrounding structures. By monitoring the morphology and particle size of the reactor products it is then possible to tailor the plasma properties and to perfect the setup in order to improve the features of the produced graphene.

3.2. Plasma characterisation

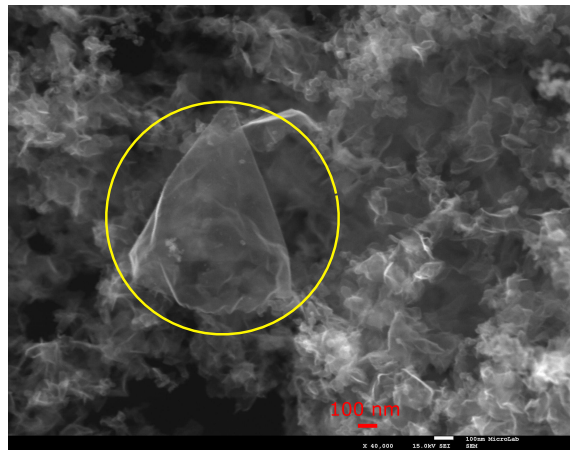
While the reactor was running we have monitored the plasma by acquiring some emission spectra before and after the precursor was introduced in the Ar plasma. By eye, a pure argon plasma shows a typical white-blueish filamentous structure; when the precursor is introduced in the reactor the plasma behaviour is characterised by repetitive bursts that are propagating from the top of the plasma towards the bottom. These bursts come with a green light (due to



(a) Tile and particle like structures.



(b) Graphene sheets mixed with other carbon allotropes and morphologies.



(c) Big carbon structure (marked with a yellow circle).

Figure 2: SEM images of the solid products obtained out of CH₄ processed by Ar plasmas

the Swan band emitted by the molecular carbon) and, at their far end, a yellow-reddish flame probably due to the Black Body emission of the solid carbon particles being produced. We have collected the plasma spectral emission using an optical fiber placed at about 5 cm from the launcher; the optical fiber is connected to a Jobin-Yvon Spex 1250 spectrometer coupled to a photomultiplier. We have calibrated the spectrometer using the peak at 546,075 nm of a Hg lamp. We have acquired a 'background' spectrum when the reactor is off: when no plasma is produced there is no appreciable signal that enters the optical fiber at any wavelength in the range from 370 nm to 770 nm. The background spectrum is therefore flat.

Fig.3 shows the spectrum of a pure Ar plasma (at atmospheric pressure). Peaks have been determined referring to NIST database [<https://www.nist.gov/pml/atomic-spectra-database>]. In Fig.4, the spectrum of Ar plasma with a 20 sccm flux of CH₄ is shown. By comparing the two spectra it is possible to notice that they are similar to each other: the only appreciable difference between them is the presence, in Fig.4, of the Swan band of the molecular carbon. It is important to mention that the intensity response of the photomultiplier has not been calibrated; as a rule of thumb, we know that, at 550 nm, the photomultiplier response is about two times that at 370 nm and seven times the response at 770 nm.

Almost all of the peaks of the plasma come from Ar ions. However, there is a couple of structure we didn't manage to identify, both around 550 nm. There is a bright peak at 546.2 nm that we cannot attribute to any atomic emission. This peak seems really close to the Hg one coming from room lamps but we didn't have it in the background spectrum. Furthermore, beside this peak, there is a broad structure that seems to be molecular.

Below the peaks, approximatively in the region between 450 nm and 700 nm, it is possible to observe a continuum spectrum coming probably from thermal bremsstrahlung and Black Body emission.

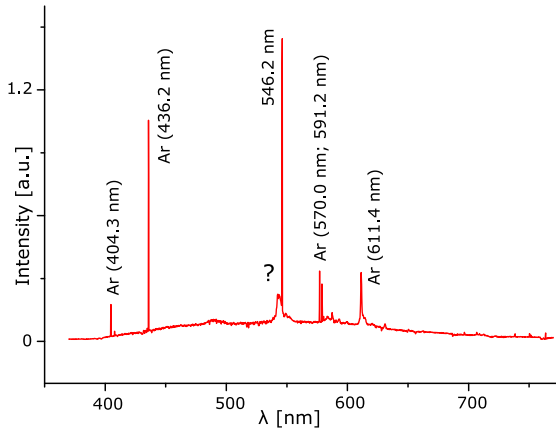


Figure 3: Emission spectrum of a pure Ar plasma

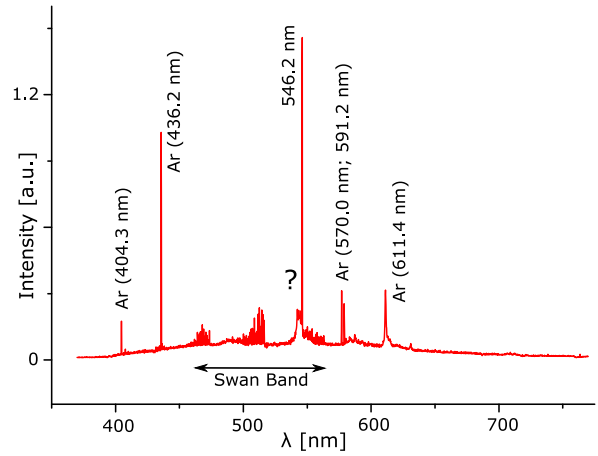


Figure 4: Emission spectrum of Ar (1200 sccm) and CH₄ (20sccm) plasma

4. Estimation of the plasma temperature by using the rotational spectrum of OH⁻

In the lab, a reliable and reproducible microwave plasma based procedure for the production of a fair amount of high quality graphene and N doped graphene has been developed during the past years [38]. Graphene is commonly produced in a dedicated setup where Ar plasma is used to process ethanol. Ethanol is injected in the plasma through the so called 'bubbling method' [41]. The setup is close to the one described in sec.2. . In addition, an in-situ annealing process is applied for oxigen reduction [37] and a UV treatment in the post-plasma zone is applied to break sp³ C bonds, increasing the sp²/sp³ ratio. [37]. As mentioned in sec.1. , controlling the thermodynamic conditions of the plasma and, in particular, the temperature, is very important to achieve an optimal control on the graphene production.

We have measured plasma temperature using the method known as 'Boltzmann plot' [43, 44, 46, 47, 48] while producing graphene in the setup mentioned above. This method assumes that Local Thermal Equilibrium (LTE) conditions are satisfied and, in particular, that the rotational temperature [49] is equal to the gas temperature. The temperature measured with this technique is an average over space (plasma column) and over time; if plasma is not stable particular care should be devoted to measurement timing. Considering a Boltzmann distribution of the atomic population, the intensity emitted due to spontaneous emission can be written as:

$$I_{rot} = aA_j \frac{hc}{\lambda_j} e^{-\frac{E_j}{kT_{rot}}}$$

where c is the light speed, h the Planck's constant, k the Boltzmann constant, a is a constant which mainly depends on the geometry of the experimental configuration and on the response of the photomultiplier, E_j is the energy of the excited level, λ_j is the wavelength of the transition and A_j is the decay probability of level j . The formula can be understood if we consider that $\frac{hc}{\lambda_j}$ is the energy of the emitted photon and $e^{-\frac{E_j}{kT_{rot}}}$ is proportional to the population in the level E_j . Hence, taking the logarithm, we get:

$$\ln\left(\frac{\lambda_j I_{rot}}{aA_j hc}\right) = -\frac{E_j}{kT_{rot}}$$

and, thus:

$$\ln\left(\frac{\lambda_j I_{rot}}{A_j}\right) = -\frac{1}{kT_{rot}} E_j + \ln\left(\frac{1}{ahc}\right)$$

from which we see that the angular coefficient of this straight line is inversely proportional to the rotational temperature of the transition.

In our measurements we are considering the rotational spectrum of OH^- whose A_j coefficient are well known. The considered transition is $A^2\Sigma^+, \nu' = 0 - X^2\Pi_i, \nu'' = 0$ (see Fig.5). A and X refer to the first electronic excited state and the ground state respectively. Symbols that follow refer to the notation: $^{2s+1}\Lambda_\sigma^p$, where s is the total electron spin about the internuclear axis, Λ is the total electron orbital momentum around the internuclear axis, p is the parity of the molecular wavefunction and σ is the symmetry of the molecular orbital [50].

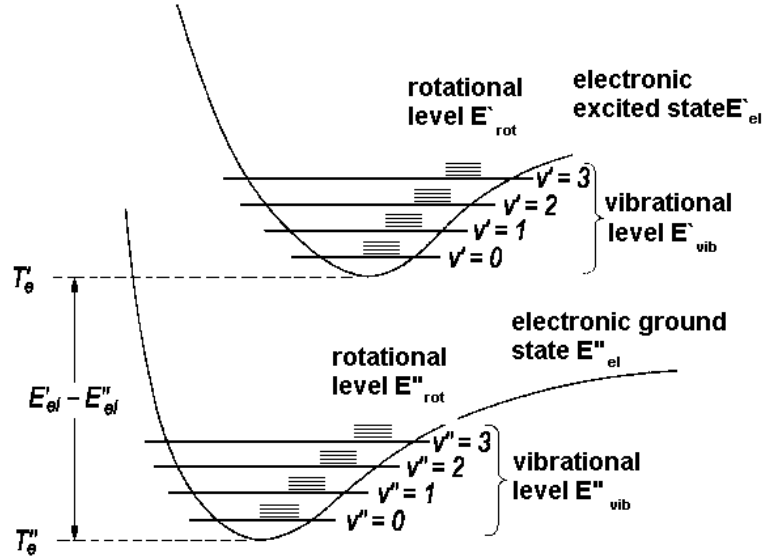


Figure 5: Schematic showing electronic, vibrational and rotational energy levels in a molecule. Rotational levels have smaller energies (about 0.001 eV) compared to the vibrational ones

We have produced graphene introducing in the plasma reactor 1200 sccm of Ar and 120 sccm of Ar and ethanol through the 'bubbling method'. We have acquired the plasma emission by positioning an optical fiber close to the reactor at about 2.5 cm from the launcher. The spectrometer grating has been calibrated as in sec.2. ; also, we have calibrated the photomultiplier intensity response. We have set the integration time for each acquired wavelength equal to 0.5 s.

In Fig.6 a plasma emission spectrum is shown. Peaks whose transition probabilities A_j are precisely known have been considered for temperature measurements and are marked with red squares in the plot. The Boltzmann plot is shown in Fig.7. The measured temperature is around 1240 K; as previously mentioned, since the LTE condition is not always satisfied, we expect an error on the plasma temperature of about 10% [46].

5. Conclusions

In our lab rotation we have had the possibility to observe and to perform several experiments. We have learned different techniques to control the plasma and to analyse the solid products obtained with a microwave plasma assisted method.

In this report, we have introduced the main features of the microwave plasma torch setup used by the N-PRiMe group to fabricate graphene and N doped graphene. Also, a preliminary analysis of the plasma and the solid products obtained during the commissioning of a microwave plasma setup have been presented. The plasma has been characterised through optical emission spectroscopy and the solid samples have been analysed by means of a scanning electron microscope. We have identified structures with the morphological characteristics of graphene mixed with 'particle-like' ones. Different morphologies have been found mixed together at different scales. Furthermore, we report the observation of a particle with a vast surface area (about 0.2 μm).

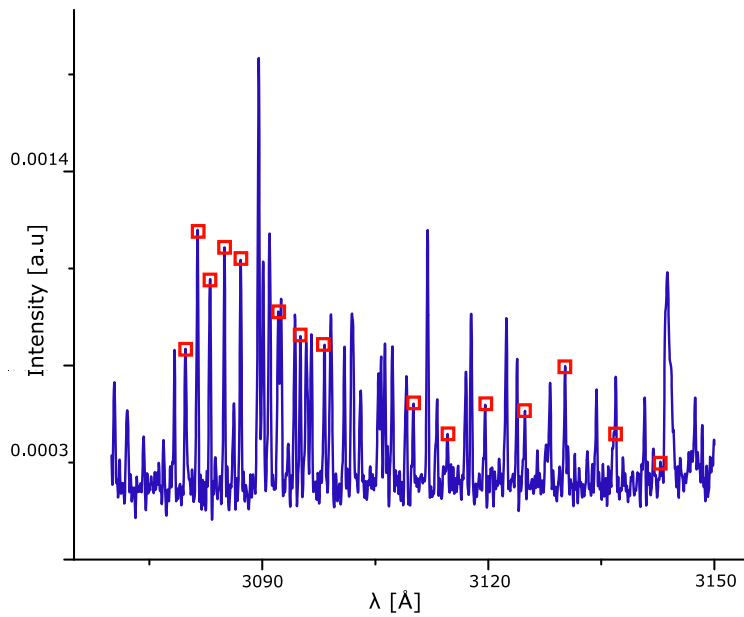


Figure 6: OH^- acquired spectrum. Red squares point at the peaks selected for temperature measurements

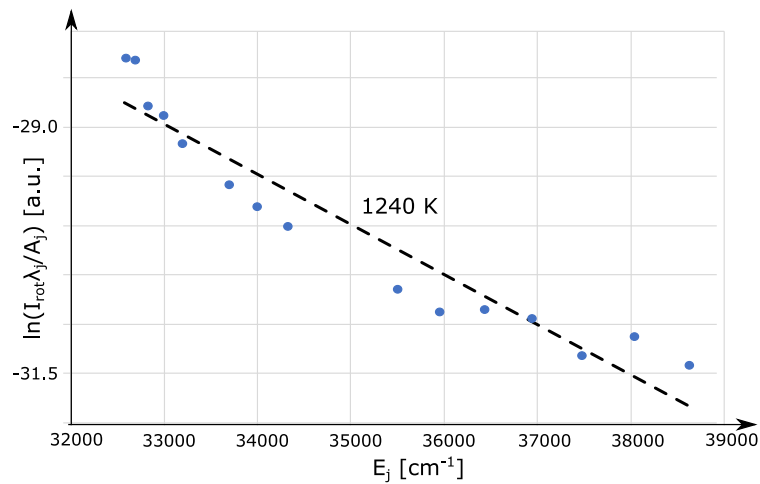


Figure 7: Boltzmann plot referring to the spectrum shown in Fig. 6

Plasma temperature has been estimated by means of the Boltzmann plot technique: the value obtained at 2.5 cm from the launcher is 1240 K.

Acknowledgements

We acknowledge prof. E. Tatarova and J. Henriques for giving us the possibility to conduct our Lab Rotation in the Plasma Engineering Laboratory and for their constant support. We thank all the PEL staff, and, in particular, E. Felizardo and N. Bundaleska for their invaluable assistance.

This work was funded by the Portuguese FCT-Fundação para a Ciência e a Tecnologia and PEGASUS Project of Horizon2020 FET-OPEN.

References

- [33] Jixin Zhu et al. ‘Graphene and graphene-based materials for energy storage applications’. In: *Small* 10.17 (2014), pp. 3480–3498.
- [34] Yangyang Wen et al. ‘Heteroatom-doped graphene for electrochemical energy storage’. In: *Chinese science bulletin* 59.18 (2014), pp. 2102–2121.
- [35] Mitchell Bacon, Siobhan J Bradley and Thomas Nann. ‘Graphene quantum dots’. In: *Particle & Particle Systems Characterization* 31.4 (2014), pp. 415–428.
- [36] Shoujun Zhu et al. ‘The photoluminescence mechanism in carbon dots (graphene quantum dots, carbon nanodots, and polymer dots): current state and future perspective’. In: *Nano Research* 8.2 (2015), pp. 355–381.
- [37] E Tatarova et al. ‘Microwave plasmas applied for the synthesis of free standing graphene sheets’. In: *Journal of Physics D: Applied Physics* 47.38 (2014), p. 385501.
- [38] E Tatarova et al. ‘Towards large-scale in free-standing graphene and N-graphene sheets’. In: *Scientific reports* 7.1 (2017), p. 10175.
- [39] E Tatarova et al. *Atmospheric Pressure Plasmas: Processes, Technology and Application*. Ed. by Margaret Parker. Nova Science Publishers, 2016. Chap. Microwave Plasmas Applied for Synthesis of Free-Standing Carbon Nanostructures at Atmospheric Pressure Conditions.
- [40] A Dias et al. ‘Production of N-graphene by microwave N₂-Ar plasma’. In: *Journal of Physics D: Applied Physics* 49.5 (2016), p. 055307.
- [41] J Henriques et al. ‘Microwave plasma torches driven by surface wave applied for hydrogen production’. In: *international journal of hydrogen energy* 36.1 (2011), pp. 345–354.
- [42] D Tsyganov et al. ‘On the plasma-based growth of ‘flowing’ graphene sheets at atmospheric pressure conditions’. In: *Plasma Sources Science and Technology* 25.1 (2015), p. 015013.
- [43] Dias A. *Microwave Plasmas Applied For Graphene Synthesis*. Master thesis, 2013.
- [44] Felizardo E. *Plasma à Pressão Atmosférica Mantido por Ondas de Superfície*. Master thesis.
- [45] M Moisan et al. ‘The waveguide surfatron: a high power surface-wave launcher to sustain large-diameter dense plasma columns’. In: *Journal of Physics E: Scientific Instruments* 20.11 (1987), p. 1356.
- [46] MC Quintero et al. ‘Determination of the excitation temperature in a nonthermodynamic-equilibrium high-pressure helium microwave plasma torch’. In: *Applied spectroscopy* 51.6 (1997), pp. 778–784.
- [47] SS Hamed. ‘Spectroscopic determination of excitation temperature and electron density in premixed laminar flame’. In: *Egypt. J. Solids* 28 (2005), pp. 349–357.
- [48] E Pawelec. ‘Estimation of the plasma temperature by using the resolved spectrum of N 2+’. In: *The European Physical Journal Special Topics* 144.1 (2007), pp. 227–231.
- [49] Peter Atkins and Julio De Paula. *Physical chemistry*. Oxford University Press, USA, 2006. Chap. 17.2.
- [50] Peter Atkins and Julio De Paula. *Physical chemistry*. Oxford University Press, USA, 2006. Chap. 14.1.

Nonlinear processes for ultrashort pulse broadening



Victor is 25 years old and he has joined APPLAuSE this year after obtaining his MSc degree in Engineering Physics in 2016 from IST, under the supervision of Dr. Gonçalo Figueira. He has been dedicated to Laser Physics in the last couple of years, namely laser-plasma interaction, laser-matter interaction, laser ablation and high-power laser science. During the last year he was awarded the Calouste Gulbenkian Foundation Prize for Stimulus to Scientific Research for his project “Fab-Laser – Femtosecond ablation of biological samples with shaped laser pulses”.

During the work at IST he participated in several physics fairs mainly giving outreach presentations to high school students to join the scientific world. Victor enjoys playing sports and reading books during his free time. He has also been evolved in volunteering work developing his creative and social skills.

Victor Hariton

Instituto de Plasmas e Fusão Nuclear (IPFN), Instituto Superior Técnico, Avenida Rovisco Pais, 1049-001 Lisboa, Portugal

E-mail: victor.hariton@ist.ulisboa.com

February 2018

Abstract.

Study and optimization of the pulse broadening technique are the main topics of this work. Spatial and temporal characterization of a beam propagation were developed using generalized ABCD matrix formalism. A split-step method was applied to predict the spectral broadening of a (ultrashort laser pulse) after interaction with material. Experimental work was carried with no significant broadening observed for singular plate configuration and a factor of 1.6 increase for multi-plate geometry was obtained.

1. Introduction

Ultrashort laser pulses have found a great variety of applications in science and technology. They have been employed in fields such as femtochemistry and -biology, laser micromachining, high-speed communication, metrology, or time-resolved spectroscopy in any type of matter [51, 52]. In particular, some applications require pulse durations of only few optical cycles, like attosecond metrology, ultrafast current switching in dielectrics or extreme ultraviolet high-harmonic spectroscopy of solids and these type of laser pulses can be routinely reached with amplifier systems [53]. However, these systems usually operate at high peak power (GW level) but low average powers ($< W$) and repetition rates (< 10 kHz). For example, Titanium doped sapphire (Ti:Sa) lasers have been exploited to generate few-cycle pulses [54] at MHz repetition rates due to their broad gain bandwidth. However, Ti:Sa oscillators can only be operated at several Watts of average power and sub- μJ pulse energies [55], and therefore, not being suited for the next generation of femtosecond technology which targets up-scaling of both average and peak power [56]. This would for instance allow better experimental conditions with higher stability conditions and faster data acquisition rates.

Nowadays, three types of lasers compete for reaching new records in combining peak and average power. These are fiber [57], innoslab [58] and thin-disk [56] technologies. Nevertheless, direct few-cycle pulse generation from any power-scalable laser system is not easy to achieve and hence external spectral broadening and pulse compression is necessary to reach the ultrashort pulse regime.

In the current state-of-the-art, first sub-10 fs pulses have been generated by means of spectral broadening in the solid-core fiber and subsequent compression of the chirped pulses [59]. This method was also successfully employed in high power architectures, resulting in compression of pulses from a sub-ps oscillator mode-locked with a semiconductor saturable absorber mirror (SESAM) to about 30 fs, sub-20 fs from a Kerr-lens mode-locked (KLM) oscillator and sub-25 fs pulses at 250 W of average power from a fiber amplifier system [60]. However, despite the success in scaling to high average power, this method is incompatible with high peak power systems due to the critical self-focusing [61]. Using the well known technique of chirped pulse amplification, peak power scalable spectral broadening became also a topic of intense research. Rolland and Corkum proposed perhaps the simplest broadening technique which is focusing intense light into a bulk plate such that the critical self-focusing length exceeds the physical length of the nonlinear medium [62]. Although the study accomplished a pulse compression from 92 fs to 19 fs and was followed by several theoretical papers discussing the method [63], the power efficiency of only about 4 % made the method unattractive for practical use. In 2000, Milosevic et al. explicitly evaluated the strengths and weaknesses of pulse broadening and compression in bulk media [64] using coupled-mode theory to analyze the spatial losses and found that broadening in solid material can only be made efficient if the peak power is much lower than the critical power of the material. These reports, referring to single-plate broadening, have been disclaimed by Lu et al. [65] who efficiently broadened ultrashort pulses with GW peak power level.

This report is structured in the following way: First we calculate the parameters that influence the broadening performance. A matrix based analytical approach is used to derive the spatial and temporal evolution of the beam inside and outside of the bulk material. Next, a simulations based on split-step method is used to predict the spectral broadening. An experimental campaign was conducted as an attempt to benchmark the theoretical predictions. Finally, all results are summarized and conclusions on the applicability of bulk broadening are drawn.

2. Theory of bulk material

To broaden a pulse filamentation is required, and the initial stage of filament formation is a result of the intensity-dependent refractive index: $n = n_0 + n_2 I$, where I is the intensity, n_0 is the linear refractive index. The nonlinear refractive index, n_2 , is related to the third-order (cubic) optical susceptibility of the material and which is positive, in the near-IR, in the transparency range of dielectric media. The induced change of the refractive index is proportional to the local intensity and thus is higher at the center of the beam and lower at the edges. Therefore the material acts like a lens, which enforces the beam to self-focus. For a cylindrically symmetric Gaussian beam the self-focusing threshold is defined by the beam critical power

$$P_{cr} = \frac{3.72\lambda^2}{8\pi n_0 n_2} \quad (1)$$

where λ is the laser wavelength; that is the power, for which the effect of self-focusing precisely balances the diffractive spreading of the beam. Spectral broadening in bulk material is not limited by the critical power. The beam collapse can be avoided if the length of the medium is smaller than the critical self-focusing length z_{sf} which is approximately:

$$z_{sf} = \frac{0.367z_R}{\sqrt{[(P/P_{cr})^{1/2} - 0.852]^2 - 0.0219}} \quad (2)$$

Here $z_R = \pi n_0 \sigma_0^2 / \lambda$ denotes the Rayleigh (diffraction) length of the input Gaussian beam of a focus σ_0 .

Assuming a 1 μm wavelength, the maximum critical power for solid materials is MW-level (5.9 MW for CaF_2 and 3.3 MW for Sapphire) and thus far below the peak powers of amplifier systems or the latest mode-locked oscillators.

We compute the beam waist necessary to reach the optimal intensity (I_0) using critical power (P_{cr}) and double of the critical power for two materials used for broadening. For these calculations, we consider a 400 fs Gaussian beam at central wavelength 1030 nm of pulse energy 1.0 mJ operating at 10 Hz. Using Eq. 1 and plates of 4 mm, 2 mm and 1 mm we present the results in Table 1.

Thickness (mm)	P_{cr}			$2P_{cr}$		
	4	2	1	4	2	1
σ_{CaF_2} (μm)	334	236	167	236	167	118
σ_{Sapph} (μm)	450	318	225	318	225	159

Table 1: Calculated beam waist necessary to reach optimal intensity for critical power and double of the critical power. The minimum damage threshold waist for the CaF_2 and Sapphire are calculated to be 86 μm and 114 μm , respectively.

3. Matrix formalism

3.1. Spatial and temporal description

We proceed with the description of beam parameters modification (temporal and spatial) after the laser-material interaction. In the ray-pulse matrix treatment the 4×4 matrices are used describe the time and space-varying beam propagation. The matrix relates the output and input of the transverse coordinate x , the propagating angle θ , the group arrival time t , and the frequency shift f as:

$$\begin{bmatrix} x \\ \theta \\ t \\ f \end{bmatrix}_{out} = M \begin{bmatrix} x \\ \theta \\ t \\ f \end{bmatrix}_{in}$$

The formalism works within the Gaussian approximation by keeping terms up to second order in powers of x and t . The only elements that combine spatial and temporal effects are the dispersive ones, i.e., the prisms, but this is not the considered case and the matrix is reduced to two 2×2 diagonal blocks as

$$M = \begin{bmatrix} A & B & 0 & 0 \\ C & D & 0 & 0 \\ 0 & 0 & K & I \\ 0 & 0 & J & L \end{bmatrix}$$

The purely spatial part of the matrices is the well-known **ABCD** matrix. The temporal part stresses the spatial-temporal analogy and we use the letters **KIJL** to describe the entrance elements. The block separation helps to simplify the calculations, but it does not imply that spatial and temporal variables are decoupled. The coupling

comes from the non-linearities in the rod through the energy of the pulse. If the off-diagonal blocks are zero, then the pulse can be described by a product of the temporal and the spatial Gaussian as

$$E(t) = \left(\frac{U}{\tau\sigma^2} \right)^{1/2} \exp(-ikr^2/2q) \exp(-ikt^2/2p).$$

with

$$\frac{1}{q} = \frac{n}{R} - \frac{in\lambda}{\pi\sigma^2} \quad (3)$$

$$\frac{1}{p} = \frac{1}{k} \frac{\partial^2 \phi}{\partial t^2} + \frac{in\lambda}{\pi\tau^2} \quad (4)$$

where n is the refractive index, λ is the central wavelength, R is the phase-front radius of curvature, σ is the beam size, τ is the pulse width, U is the energy, and ϕ is the phase. After a system is crossed with a matrix defined by the ABCD and KIJL blocks, the output pulse results, with parameters q_{out} and p_{out} given in terms of the input parameters q_{in} and p_{in} by

$$q_{out} = \frac{\mathbf{A}q_{in} + \mathbf{B}}{\mathbf{C}q_{in} + \mathbf{D}} \quad (5)$$

$$p_{out} = \frac{\mathbf{K}p_{in} + \mathbf{I}/\lambda}{\lambda\mathbf{J}p_{in} + \mathbf{L}} \quad (6)$$

For the spatial treatment, taking into account the Kerr lens effect, we define the propagation matrix as

$$M_1 = \begin{bmatrix} A & B \\ C & D \end{bmatrix} = \begin{bmatrix} 1 & 0 \\ C & 1 \end{bmatrix}$$

where

$$Re(\mathbf{C}) = -\frac{4n_2UL}{\tau\sigma^4} \left(\frac{2}{\pi} \right)^{3/2}, \quad (7)$$

L being the rod thickness. In Fig. 1 we show the predicted laser beam waist after a propagation through 5 bulk mediums with different thicknesses. The separation distances are derived allowing the beam size to recover in air returning to similar values calculated in the previous section (Table 1). The compiled results are presented in Table 2. The Sapphire plate thicknesses used in this simulation are 4mm, 2mm, 2mm, 1mm and 1mm from left to right respectively.

Spacing between plates (mm)			
1 to 2	2 to 3	3 to 4	4 to 5
12	7	3.5	15

Table 2: Retrieved distances between plates for a 5 plate system. Red lines indicate the position of the Sapphire plates. Thicker plates (4mm) are placed first and thinner(1mm) last. The final configuration being 4-2-2-1-1.

A similar approach was used in attempt to predict the time change and the pulse spectral broadening of a laser beam crossing a bulk material. With the submatrix **KIJL** given by

$$M_2 = \begin{bmatrix} K & I \\ J & L \end{bmatrix} = \begin{bmatrix} 1 & I \\ J & 1 \end{bmatrix}$$

where I is the group-velocity dispersion (GVD) and the self-phase modulation (SPM) is given by

$$\mathbf{J} = \frac{4n_2UL}{\lambda\tau^3\sigma^2} \left(\frac{2}{\pi} \right)^{3/2}. \quad (8)$$

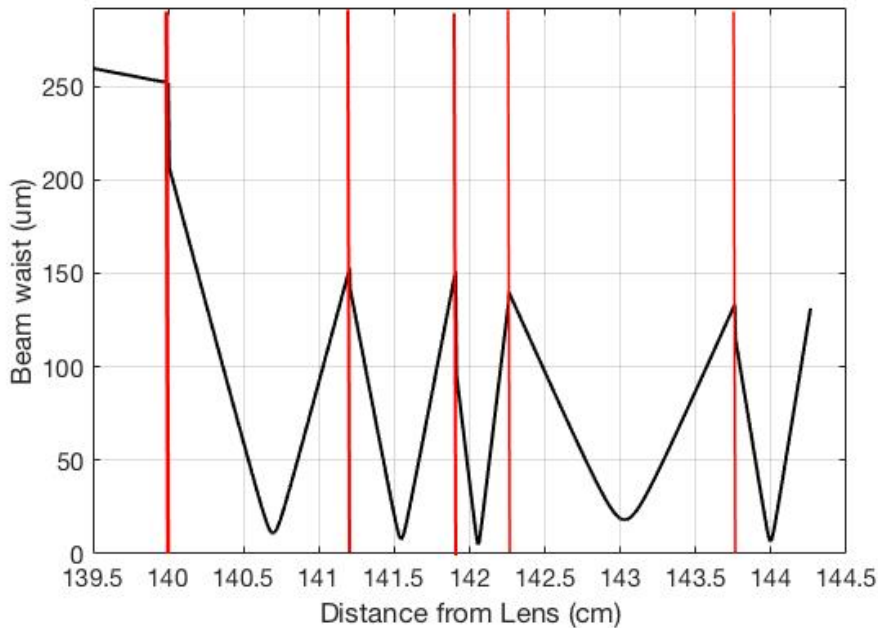


Figure 1: Simulated beam waist propagation through 5 Sapphire plates. Kerr lensing and divergence are the only effects taken into consideration. Thicker plates (4mm) are placed first and thinner(1mm) last. The final configuration being 4-2-2-1-1.

Although the result was qualitatively correct, our simplified model rod overestimated the non-linearity and we could not benchmark, so far, the simulation results with reported data presented in the literature. Nevertheless, a matrix formalism has been presented that takes into account the most important features of non-linear laser material interaction.

4. Split-step method for time domain

Due to the lack of success in using the matrix approach to predict the spectral broadening, another numerical method was implemented. The split-step method is well-known to numerically describe the solutions, of the self-phase modulation equation, of the pulse propagation in a bulk material. It consists in considering firstly only the linearities in the equation by discrete Fourier transformation and then secondly only the nonlinear terms.

While the construction of such split-step Fourier methods (SSFM) is very well established for different physical processes and materials, namely optical fibers [66], the topic of how to describe the interaction with thin bulk material has received little attention. Here, we constructed a numerical code that is able to predict the pulse temporal and spectral broadening after crossing thin slabs of material.

The simulated input and output spectra are showed in Fig. 2a-2b. We show the results for two time durations, in particular a 200 fs pulse and a 400 fs pulse. Both pulses have 1 mJ of energy and $1.03 \mu\text{m}$ of wavelength. The simulated material is a Sapphire rod of 1 cm of thickness (equivalente of the 5 plates from the previous section) with a non-linear index of $n_2 = 2.8 \times 10^{-20} \text{ W/m}^2$.

We observe higher broadening for the 200 fs pulse, due to the increase of the non-linearity. We predict an approximately 30 times increase of the bandwidth in this case and a 15 times in the case of the 400 fs pulse duration.

Furthermore, the whole evolution along the thickness of the material rod can be visualized in Fig. 3a and Fig. 3b. Comparable results were obtained in previous work [67] which confirms the accuracy of the developed code.

Moreover, it is not enough to increase the available bandwidth of the pulse, it is also important to maintain the current time duration. The two regimes simulated show that for long pulses (400 fs, Fig. 4b), 1 cm of material

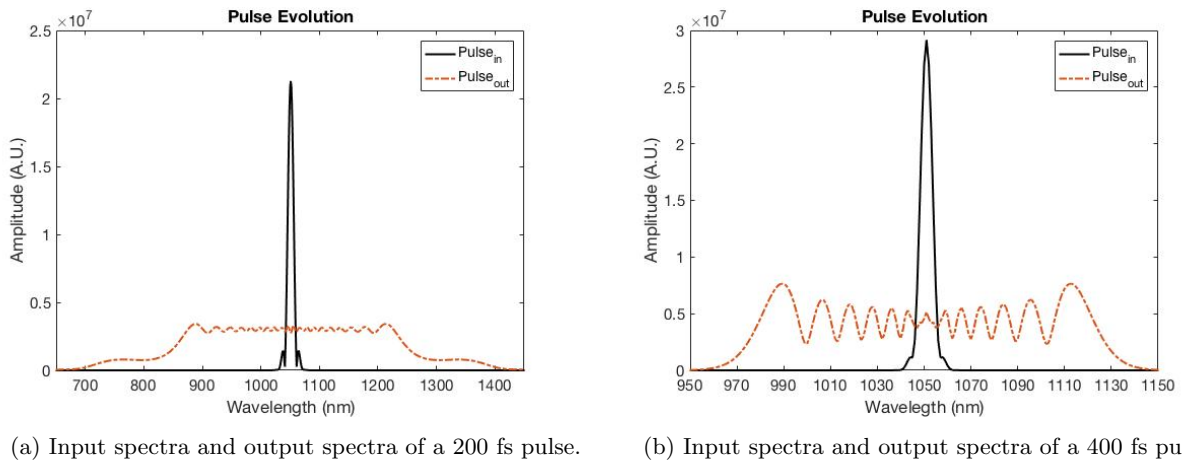


Figure 2: Spectral comparison between initial and final pulse after 1cm Sapphire interaction.

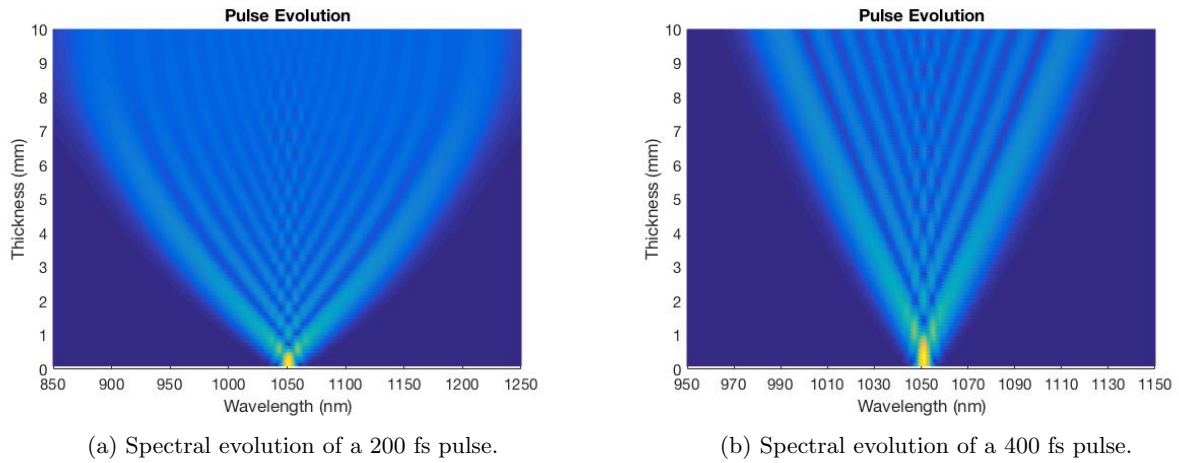


Figure 3: Spectral evolution inside the material of two different time scale pulses. Shorter pulses present higher broadening ratio.

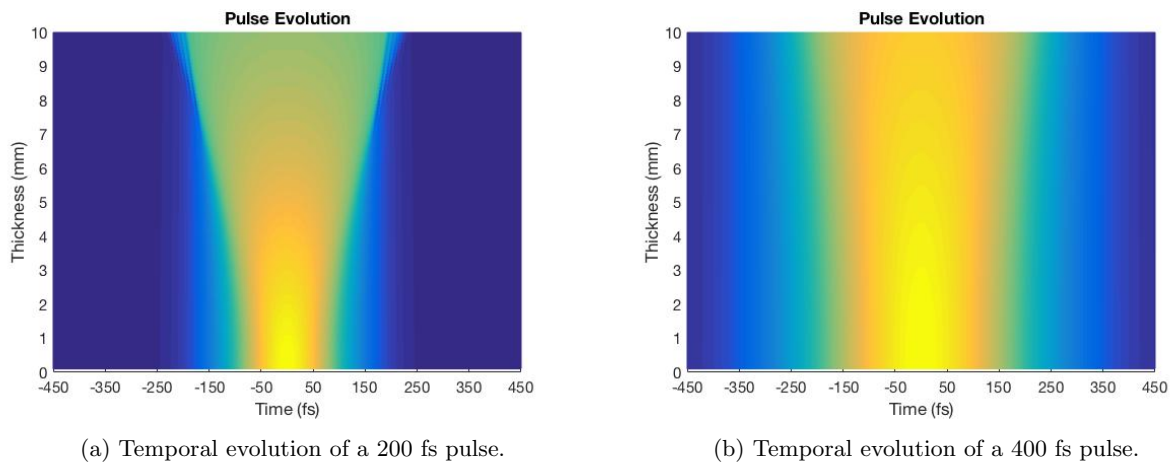


Figure 4: Temporal evolution inside the material of two different time scale pulses. Shorter pulses present higher temporal dispersion.

generates low dispersion, while for shorter pulses, Fig. 4a the GVD is significant and broadens temporally the incident pulse.

5. Experimental setup and results

Experimental work was conducted in order to confirm the simulated results. The output of a regenerative amplifier is used which delivers laser pulses with ≈ 400 fs, 1.5 mJ at 10 Hz. The IR pulses are focused on different material by using 150 cm focal length. The schematic of the pulse broadening technique with only two plates is shown in the figure 5a.

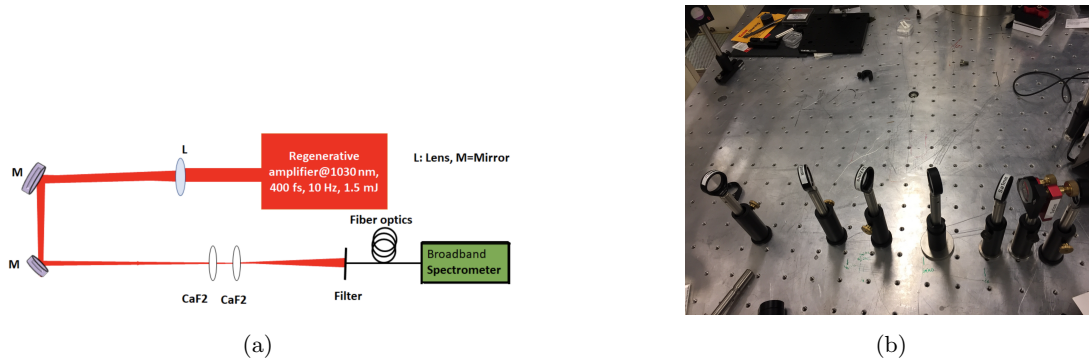


Figure 5: Schematic of multiple plates pulse broadening setup.

Several architectures were tested. In order to find the ideal beam size position a camera was used to scan the waist. Singular plate broadening was attempted using plates of Sapphire and CaF_2 ranging from 4 mm to 1 mm placed in different focal spot without damaging. No significant broadening was observed even though the critical power was surpassed.

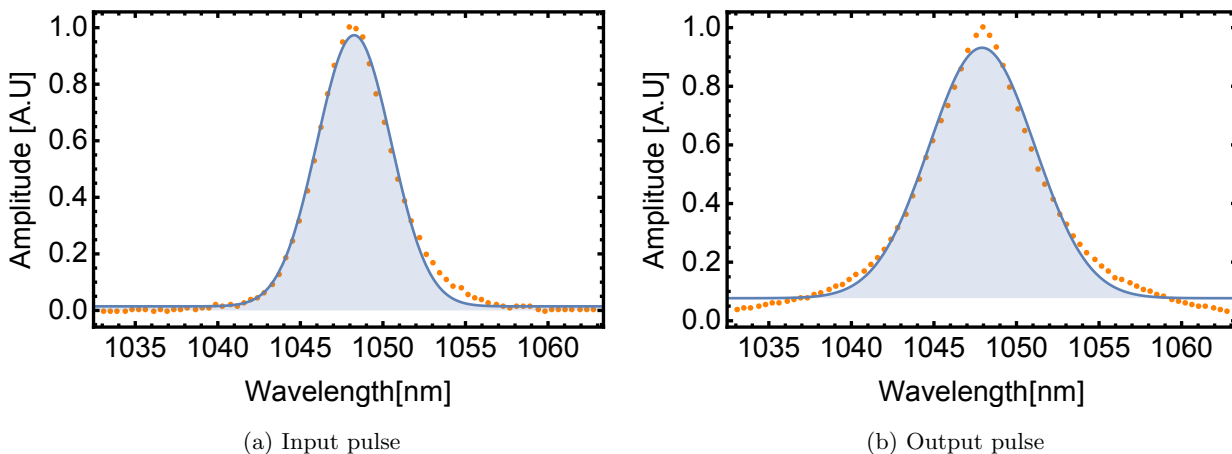


Figure 6: Measured multi-plate broadening of the laser pulse. Total thickness summing to 2.5 cm of material. A broadening factor of 1.6 was retrieved.

To continue the campaign, a multi-plate broadening geometry was implemented. The first plate was placed at the corresponding position where the maximum broadening is observed. It was shown that the transmitted beam focuses after the first plate, and taking this into account the next plates were placed according to the simulations, with separations ranging from several mm's to 1 cm, avoiding optical damage.

The comparison between the input and output beam can be visualized in Figure 6a and 6b. An increase by a factor of 1.6 is observed when all of the plates are used, in total 2.5cm of bulk material. The bandwidth stretches to 8 nm starting from 4.95 nm. The measured efficiency of this process is of over 60% when the used plates are

placed in the Brewster angle. The results are not what it is expected and optimization was performed but without significant success.

6. Conclusion

The goal of the laboratory work was to investigate the feasibility of a simple pulse broadening stage applied to the ultrafast laser. Efficient and scalable broadening was expected using multi-slab approach. In order to achieve this, a beam propagation routine based on Kerr lens effect was developed using the ABCD matrix method. A similar approach was used for temporal domain, not achieving the same accuracy. Moreover, spectral broadening equations were solved using split-step method, achieving comparable to literature results. An experimental setup was constructed in order to observe the broadening effect in singular and multi-slab regime. No conclusive results were retrieved so far. A maximum broadening by a factor of 1.6 was achieved, far below the expected value. The possible reasons behind these findings could be the oversimplification of the model by not considering other effects and imperfect experimental conditions. Future work must be carried on to fully understand the dominating effects in the process.

References

- [51] N. Bloembergen. ‘From nanosecond to femtosecond science’. In: *Rev. Mod. Phys.* 71 (2 1999), S283–S287. DOI: 10.1103/RevModPhys.71.S283. URL: <https://link.aps.org/doi/10.1103/RevModPhys.71.S283>.
- [52] Rafael R. Gattass and Eric Mazur. ‘Femtosecond Laser Micromachining in Transparent Materials’. In: 2 (Apr. 2008), pp. 219–225.
- [53] Thomas Brabec and Ferenc Krausz. ‘Intense few-cycle laser fields: Frontiers of nonlinear optics’. In: *Rev. Mod. Phys.* 72 (2 2000), pp. 545–591. DOI: 10.1103/RevModPhys.72.545. URL: <https://link.aps.org/doi/10.1103/RevModPhys.72.545>.
- [54] Franz X Kärtner. *Few-cycle laser pulse generation and its applications*. Vol. 95. Springer Science & Business Media, 2004.
- [55] S Naumov et al. ‘Approaching the microjoule frontier with femtosecond laser oscillators’. In: *New Journal of Physics* 7.1 (2005), p. 216. URL: <http://stacks.iop.org/1367-2630/7/i=1/a=216>.
- [56] Hanieh Fattahi et al. ‘Third-generation femtosecond technology’. In: *Optica* 1.1 (2014), pp. 45–63. DOI: 10.1364/OPTICA.1.000045. URL: <http://www.osapublishing.org/optica/abstract.cfm?URI=optica-1-1-45>.
- [57] Jens Limpert. ‘High Power Fiber Lasers’. In: *Optical Fiber Communication Conference*. Optical Society of America, 2017, W1F.5. DOI: 10.1364/OFC.2017.W1F.5. URL: <http://www.osapublishing.org/abstract.cfm?URI=OFC-2017-W1F.5>.
- [58] P. Russbueldt et al. ‘Innoslab Amplifiers’. In: *IEEE Journal of Selected Topics in Quantum Electronics* 21.1 (2015), pp. 447–463. ISSN: 1077-260X. DOI: 10.1109/JSTQE.2014.2333234.
- [59] Andrius Baltuška et al. ‘Optical pulse compression to 5 fs at a 1-MHz repetition rate’. In: *Opt. Lett.* 22.2 (1997), pp. 102–104. DOI: 10.1364/OL.22.000102. URL: <http://ol.osa.org/abstract.cfm?URI=ol-22-2-102>.
- [60] T. Südmeyer et al. ‘Nonlinear femtosecond pulse compression at high average power levels by use of a large-mode-area holey fiber’. In: *Opt. Lett.* 28.20 (2003), pp. 1951–1953. DOI: 10.1364/OL.28.001951. URL: <http://ol.osa.org/abstract.cfm?URI=ol-28-20-1951>.
- [61] A. V. Smith et al. ‘Optical Damage Limits to Pulse Energy From Fibers’. In: *IEEE Journal of Selected Topics in Quantum Electronics* 15.1 (2009), pp. 153–158. ISSN: 1077-260X. DOI: 10.1109/JSTQE.2008.2010331.
- [62] Claude Rolland and P. B. Corkum. ‘Compression of high-power optical pulses’. In: *J. Opt. Soc. Am. B* 5.3 (1988), pp. 641–647. DOI: 10.1364/JOSAB.5.000641. URL: <http://josab.osa.org/abstract.cfm?URI=josab-5-3-641>.

- [63] P. Chernev and V. Petrov. ‘Self-focusing of short light pulses in dispersive media’. In: *Optics Communications* 87.1 (1992), pp. 28–32. ISSN: 0030-4018. DOI: [https://doi.org/10.1016/0030-4018\(92\)90036-Q](https://doi.org/10.1016/0030-4018(92)90036-Q). URL: <http://www.sciencedirect.com/science/article/pii/003040189290036Q>.
- [64] Nenad Milosevic, Gabriel Tempea and Thomas Brabec. ‘Optical pulse compression: bulk media versus hollow waveguides’. In: *Opt. Lett.* 25.9 (2000), pp. 672–674. DOI: 10.1364/OL.25.000672. URL: <http://ol.osa.org/abstract.cfm?URI=ol-25-9-672>.
- [65] Chih-Hsuan Lu et al. ‘Generation of intense supercontinuum in condensed media’. In: *Optica* 1.6 (2014), pp. 400–406. DOI: 10.1364/OPTICA.1.000400. URL: <http://www.osapublishing.org/optica/abstract.cfm?URI=optica-1-6-400>.
- [66] Govind P Agrawal. ‘Nonlinear fiber optics’. In: *Nonlinear Science at the Dawn of the 21st Century*. Springer, 2000, pp. 195–211.
- [67] Audrius Dubietis et al. ‘Ultrafast supercontinuum generation in bulk condensed media’. In: *Lithuanian Journal of Physics* 57.3 (2017), pp. 113–157.

Will the diagnostics components of DEMO survive long-term neutron irradiation?



Yohanes was born in Malang, East Java, Indonesia, in 1988. He got his bachelor degree from the physics department of Institut Teknologi Bandung (ITB) in 2011. He got an opportunity to learn computational fluid dynamics (CFD) and the mixed convection heat transfer during his study in the Nuclear and Quantum Engineering (NQE) department of Korea Advanced Institute of Science and Technology (KAIST) (2013-2015) with RCA-KAIST scholarship. He is interested in nuclear fusion and computational physics and open to learn other topics as well.

Yohanes S. Nietiadi

Physics Department, Instituto Superior Técnico (Universidade de Lisboa), Av. Rovisco Pais 1, 1049-001, Lisbon, Portugal

E-mail: yohanes.nietiadi@tecnico.ulisboa.pt

February 2018

Abstract.

DEMO is a proposed nuclear facility that aims at bridging the gap between ITER and the first commercial fusion power station. The diagnostics components of DEMO will face a harsh neutron and gamma radiation environment during the operation of DEMO, which can damage their materials. Thus a study for the long-term durability of these components is mandatory. MCNP6, which is the accepted code for nuclear analysis of ITER and DEMO, was used to perform a study on the long-term durability of these components. In this paper we perform an assessment of the irradiation conditions, by estimating quantities such as neutron and gamma fluxes, energy deposition, and displacement per atom (DPA). A complete assessment of the long-term durability of the diagnostics components requires a complex, multidisciplinary study, which is not in the scope of this study.

1. Introduction

DEMO (DEMOstration Power station) is a proposed nuclear power station which aims at bridging the gap between ITER and the first commercial fusion power station. DEMO is scheduled to operate during 20 calendar years (CY) with 30% of average availability, which equals to 6 full power years (FPY) [68]. This operation time will have 2 phases: 5.2 CY (1.57 FPY) in the first phase and 14.8 CY (4.43 FPY) in the second phase, the blanket modules will be changed between the two phases. The diagnostics systems of DEMO have not been decided and are still under study. In the current design stage, the assessment of the long-term durability of the DEMO diagnostics components is mandatory, since the components will face a harsh neutron and gamma radiation environment during the operation of DEMO which can damage their materials.

This study aims at assessing the irradiation conditions through the estimation of quantities such as neutron and gamma fluxes, energy deposition, and displacement per atom (DPA), defined as the number of times that an atom is displaced for a given fluence (total integral over time of neutron flux density), following the guidelines from EUROFUSION[68].

MCNP6 (Monte Carlo N-Particle 6) [69] is the accepted code for nuclear analysis of ITER and DEMO. The DEMO 2017 neutronics reference model, used in this work to perform the simulations with MCNP6 code, is shown in Fig. 1. To do the analysis on the diagnostics components, an opening in the blanket was introduced and a dummy antenna, which represents the diagnostics component, was added to the opening. These two parts (opening and antenna) are the focus of this study.

The objective of this study is to learn the tools and methods to assess the durability of the diagnostics components of DEMO by calculating DPA in the simplified antennas. In this paper, swelling is chosen as an example to show the effect of the DPAs on the mechanical properties of the materials. Other effects of neutron irradiation, such as conductivity changing, hardening, embrittlement, etc. are not in the scope of this study.

2. Methodology

2.1. Basic Geometry

This study started with the implementation of a simple geometry, materials, and the introduction of tallies and mesh tallies (detectors) to obtain the output quantities that we want to assess (neutron and gamma fluxes, energy deposition, and DPA), following the MCNP6 User's Guide [2].

2.2. DEMO 2017

The next step was to introduce an opening in one of the blankets (in the low-field side at the equatorial level) of DEMO 2017 neutronics reference model shown in Fig. 1. An "antenna", which geometry has been simplified to a cylindrical pipe with 2mm thickness. Three different diameters were tested for the opening (no opening, 5cm, and 10cm). After introducing the opening and the antenna, the displacement cross-section of stainless steel (SS-316 and EUROFER) were applied to the cell flux for the calculation of DPA and compare the irradiation effect on both materials.

3. Results and Discussion

3.1. Basic Geometry

The geometry shown in Fig. 2 is composed by a combination of basic planes to form the surfaces of the cells of the system. Materials are assigned to the cells and the effect of neutron irradiation from an extended isotropic source (cell 1), which enclosed by graphite tube (cell 2), in shield (cell 4 to 8) material of water, BeO, iron, and lead has been simulated and analyzed. Fig. 3 shows the neutron flux distribution and Fig. 4 shows the comparison of the total neutron fluxes with different shielding materials. In this case, water is the best shielding material for neutrons, since the mass of the hydrogen atom is comparable to the mass of the neutron and therefore the neutron can lose all

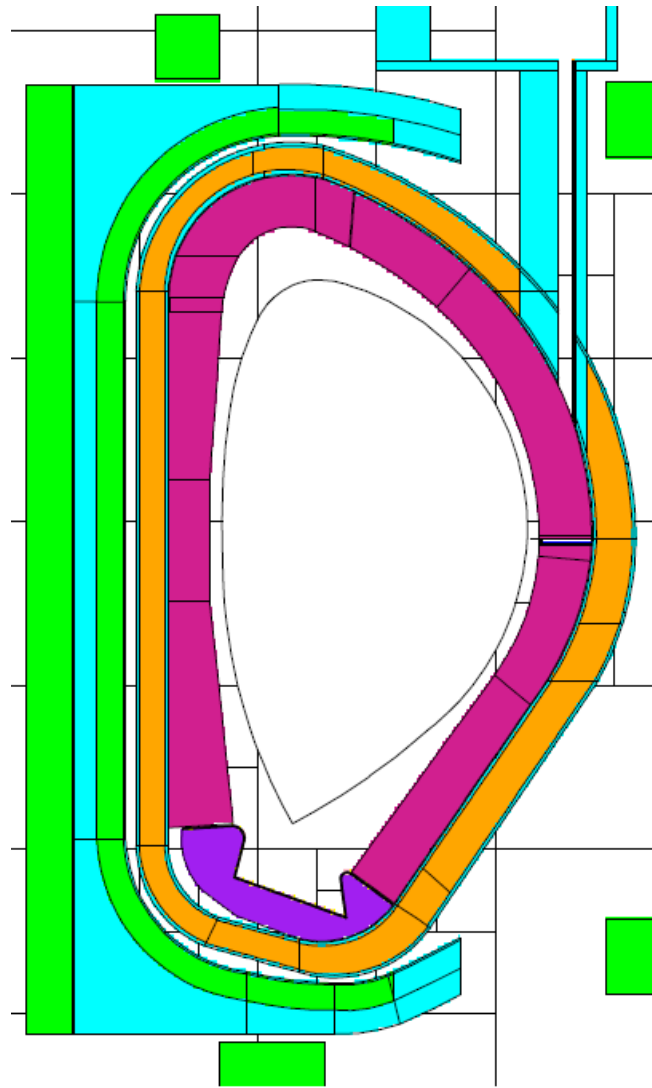


Figure 1: DEMO 2017 neutronics reference model.

its energy in a single elastic scattering collision. The other important result is that, even though the atomic mass of iron is much heavier than the one of beryllium, iron is a better neutron shield due to its higher density (although the neutrons lose less energy per collision, there are more collisions with iron nuclei than with beryllium nuclei).

3.2. DEMO 2017

The reference model of DEMO is shown in Fig. 1. In this model, an opening was introduced in one of the blankets (at the equatorial level in the low-field side), to be used for the introduction of diagnostics. In this opening, sample materials were introduced in two positions: close to the first wall and at the back of the blanket, shown in Fig. 5. These sample materials are the ones used in the reflectometry systems and are introduced here as very simplified versions of the plasma-facing antennas.

The neutron radiation source is the plasma and it radiates isotropically. The estimated neutron and gamma fluxes inside the reactor are shown in Fig. 6 and Fig. 7, respectively, while Fig. 8 shows the energy deposition in the blankets and remaining components.

From Fig. 6, we can see that the neutron source is located at the center of the geometry. The gamma fluxes, shown in Fig. 7 are, as expected, concentrated in the divertor section, which is made of tungsten (a very high-density material) that can become a gamma radiation sources when it interacts with neutron. In the opening and

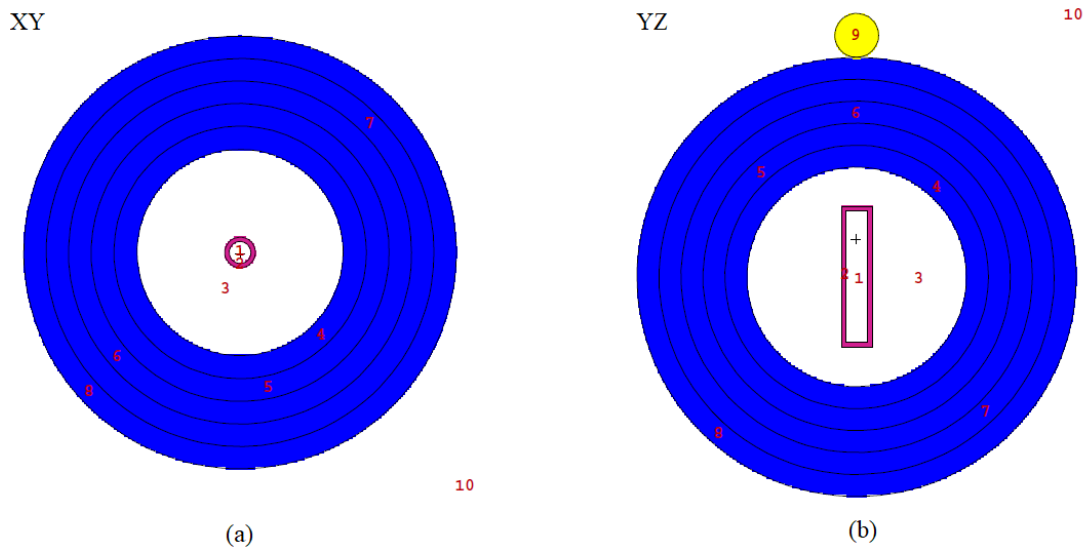


Figure 2: Basic geometry (a) XY-plane, (b) YZ-plane.

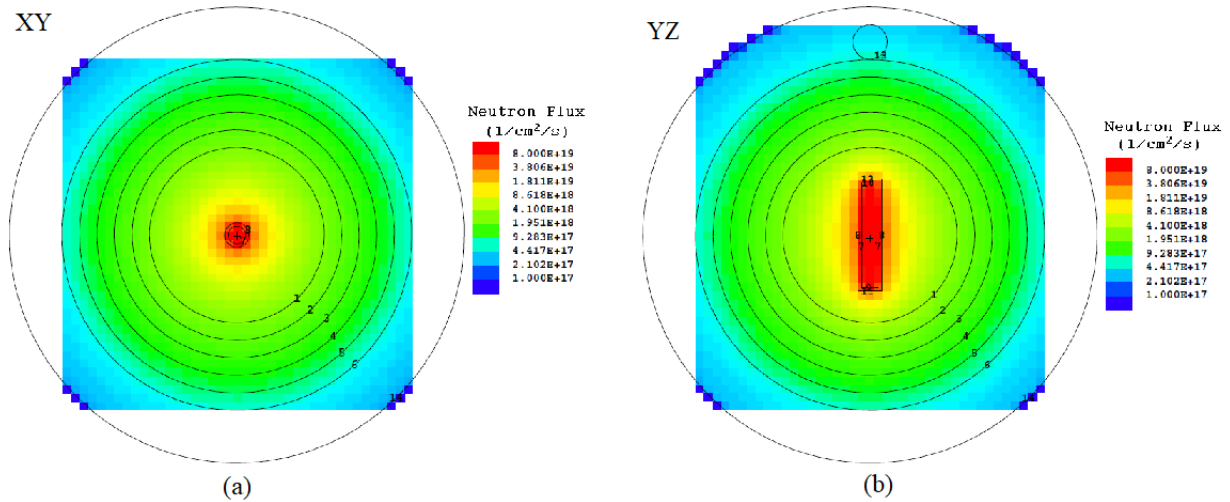


Figure 3: Neutron flux in basic geometry with water as shielding material (a) XY-plane, (b) YZ-plane.

in the antenna, the gamma flux is much lower than the neutron flux, so we can say that the irradiation received by the diagnostics system is mainly from neutrons.

The calculation of displacement per atom (DPA), which contain the important information of the material durability, follows Eq. 1,

$$N_d = N_0 \varphi \sigma_d t \quad (1)$$

where N_d is the number of atom displaced by the irradiation, N_0 is the number of the neutron irradiation, φ is the neutron flux, σ_d is the displacement cross-section, and t is the irradiation time. The heat load distribution, as expected, shows that the material facing the plasma will have higher heat loads compared to the one in the back. We can also expect that the antenna located close to the first wall will have higher DPAs compared to the one on the back.

The calculated DPAs for two phases with three different openings for EUROFER and SS-316 of the front end and the back of the antenna are presented in Fig.9 and Fig.10. The calculated results of DPA agree with the estimations of EUROFUSION for the first wall (20 DPA for the 1st phase and 50 DPA for 2nd phase) within $\sim 10\%$ for the 1st phase and within $\sim 20\%$ for 2nd phase [68].

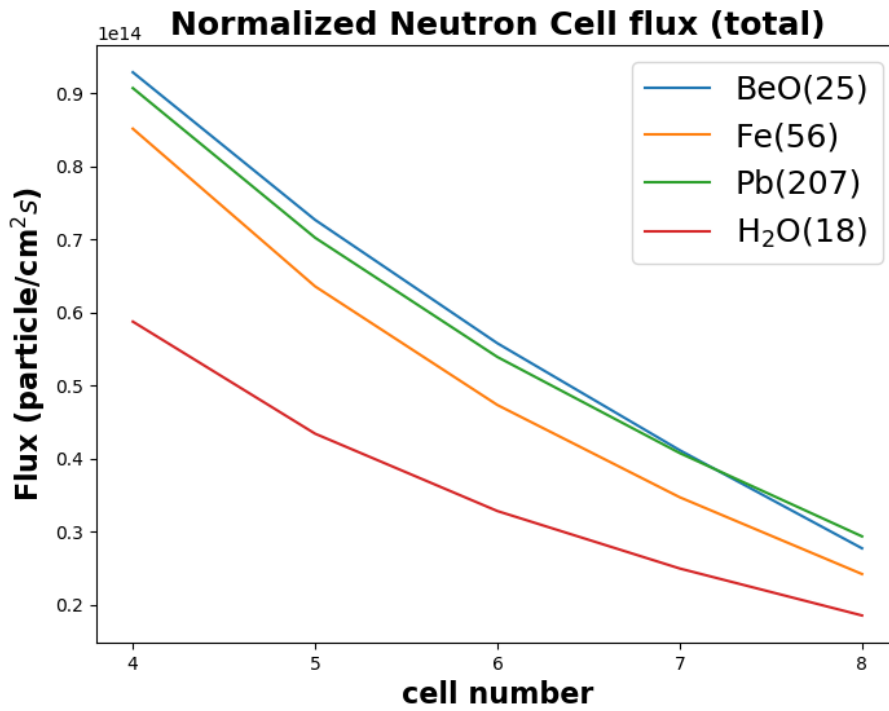


Figure 4: Comparison of the total neutron flux with different shielding materials as a function of the cell number (from the smaller radius to the larger radius).

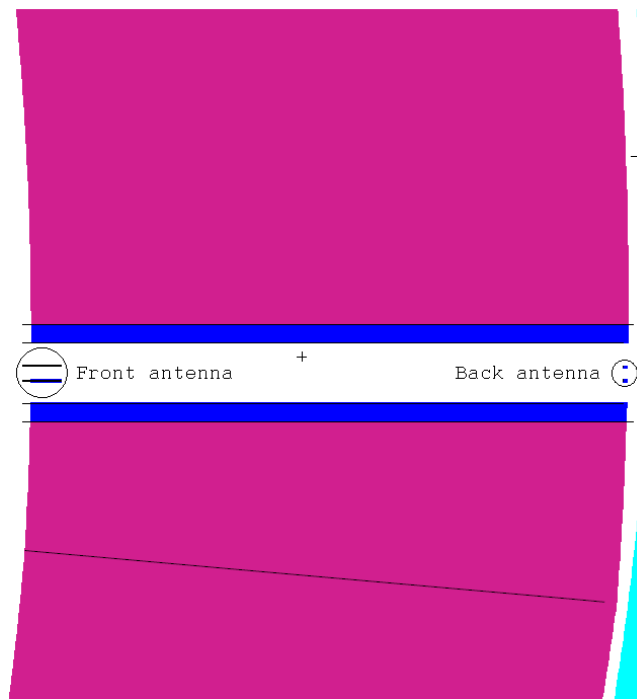


Figure 5: Relative position of the opening and antenna.

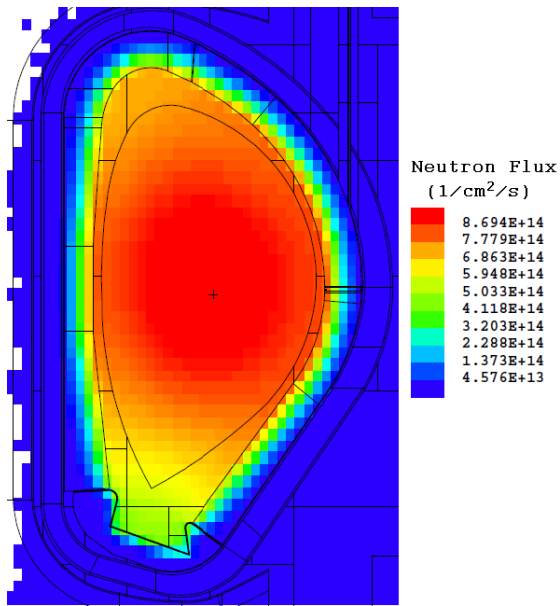


Figure 6: Estimated neutron flux of DEMO ($1/cm^2/s$).

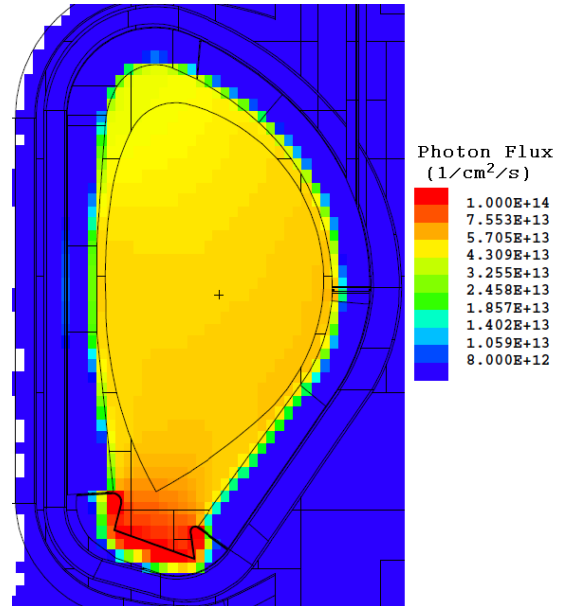


Figure 7: Estimated photon flux of DEMO ($1/cm^2/s$).

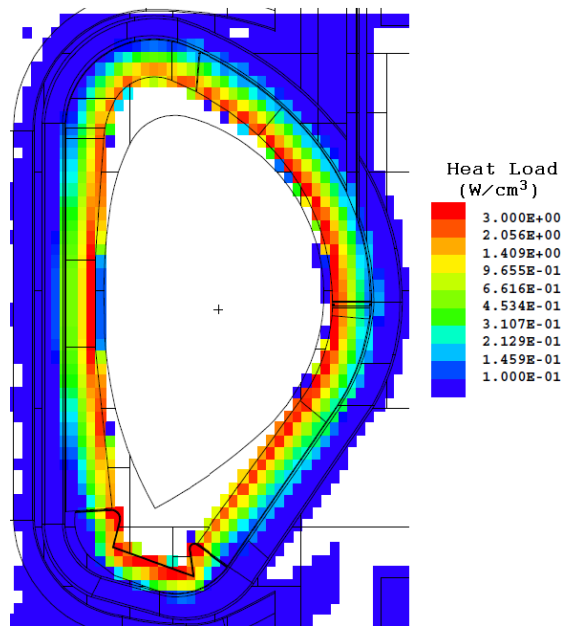


Figure 8: Estimated heat load of DEMO (W/cm^3).

For the assessment of the effect of the calculated DPAs on the mechanical properties of the materials, swelling was selected as an example. As the reflectometry components of DEMO are aimed to operate below $450^\circ C$, they will, according to Fig. 11, have more than 6% of volume swelling [70]. Swelling is only one of the effects that comes up with the irradiation of the materials; for a complete assessment of the effect of the DPAs on the mechanical properties of the materials, a complex, multidisciplinary study is required, which is not in the scope of this study.

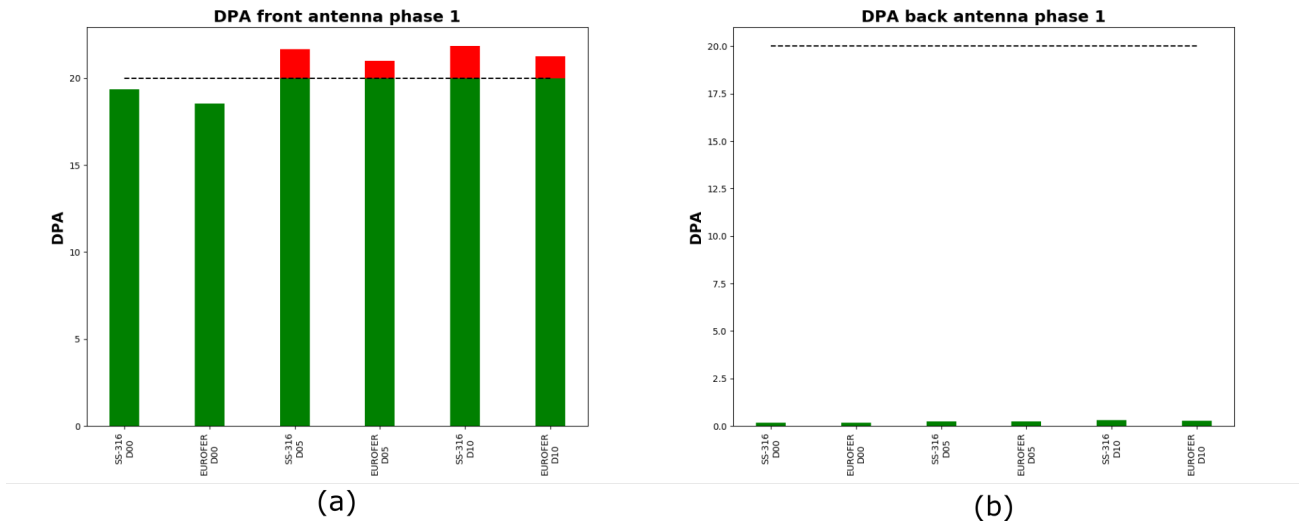


Figure 9: DPA calculation for 1st phase operation of DEMO (1.57 FPY) for: (a) front antenna, (b) back antenna.

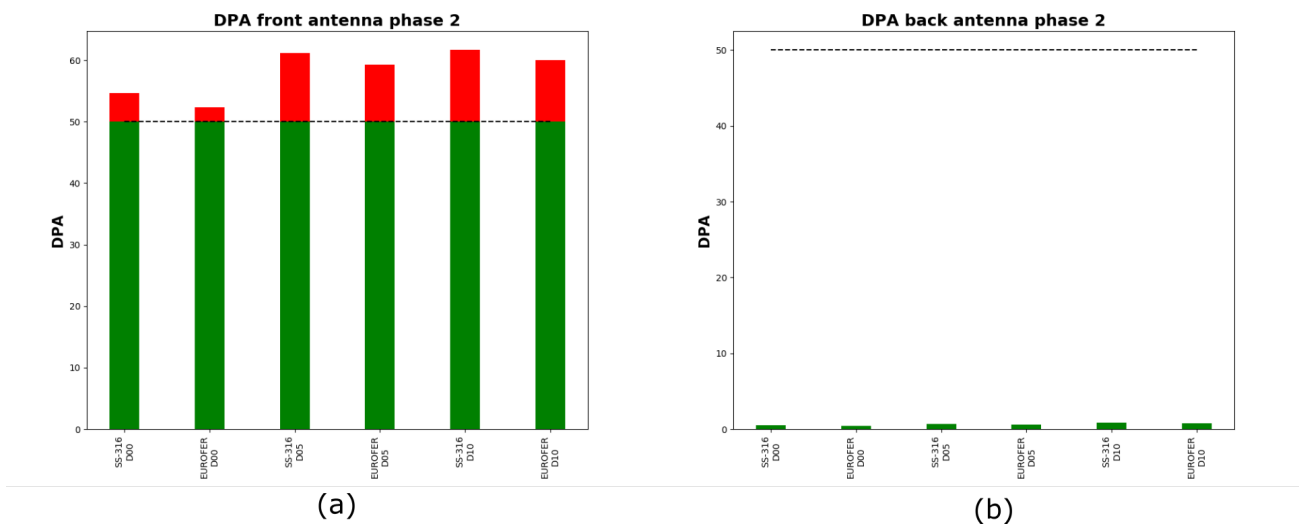


Figure 10: DPA calculation for 2nd phase operation of DEMO (1.57 FPY) for: (a) front antenna, (b) back antenna.

4. Conclusion

In this study, we presented the effects of neutron streaming to different materials. It has been found that heavy materials, such as iron, can be better neutron shields than beryllium oxide, because the density of iron is much higher than the density of BeO.

Also, the irradiation effect to the diagnostics components of DEMO is analyzed with different openings and exposure period for SS-316 and EUROFER. One can expect more damage to the diagnostics components from the larger the opening, because the total number of neutron interacts with the material will be increased.

The study of the opening and antenna in the blanket of DEMO shows that even with a simplified geometry, we can get an estimation of the received damage with 10 to 20% of deviation from previous estimations which corresponds to ~6% of diagnostics components volume swelling operated at 430°C.

In the future, more complex and multidisciplinary analysis will be done to find out if the diagnostics components of DEMO will survive.

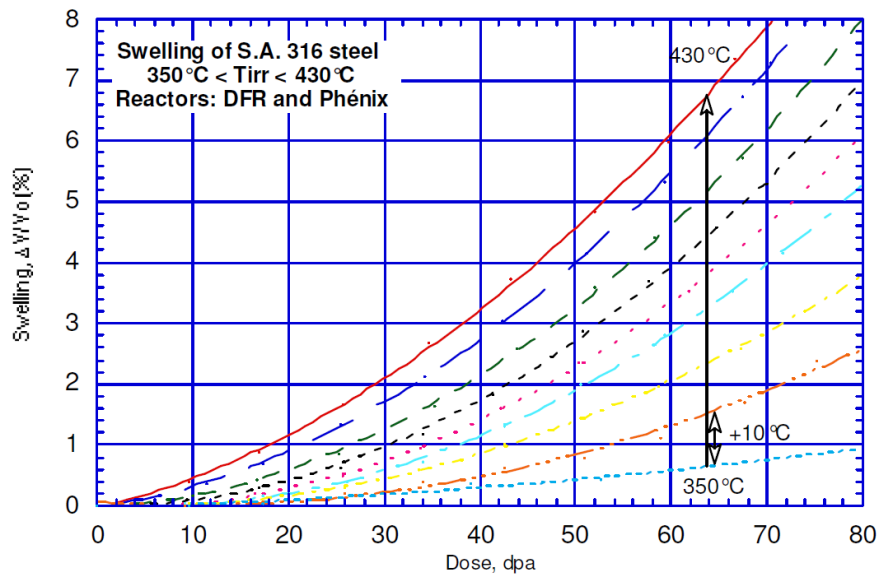


Figure 11: Swelling law for irradiation temperature from 350°C to 430°C with 10°C difference for each different line (S.A. - solution annealed) [70].

References

- [68] U. Fischer. Guidelines for Neutronic Analyses EUROFUSION. 2016.
- [69] Team MCNP6. MCNP6 User's Guide. 2013.
- [70] V. Barabash. Appendix A. Material Design Limit Data. 2013.

